NASA Technical Paper 2679

May 1987

Experimental Validation of a Two-Dimensional Shear-Flow Model for Determining Acoustic Impedance

Tony L. Parrott,
Willie R. Watson,
and Michael G. Jones

NASA

NASA Technical Paper 2679

1987

Experimental Validation of a Two-Dimensional Shear-Flow Model for Determining Acoustic Impedance

Tony L. Parrott
and Willie R. Watson
Langley Research Center
Hampton, Virginia

Michael G. Jones
PRC Kentron, Inc.
Hampton, Virginia

National Aeronautics
and Space Administration

Scientific and Technical Information Branch

Summary

Tests were conducted to validate a two-dimensional shear-flow analytical model for determining the acoustic impedance of an acoustic liner test specimen in a grazing-incidence, grazing-flow environment using the infinite-wave-guide method. The test specimen consisted of a rigid matrix of small-diameter circular channels acoustically isolated from one another. This particular test specimen structure was chosen to minimize grazing-flow effects so that the analytical model could be expected to produce results nearly the same as normal-incidence impedance measurements.

The analytical model was exercised at three levels of flow profile model complexity: a uniform (or "plug") flow model, a one-dimensional shear-flow model, and a two-dimensional shear-flow model. Impedances for both downstream and upstream sound propagation generally agreed well with the normal-incidence impedances for all levels of flow profile model complexity. Consistency of the results suggests that if due consideration is given to the effects of variability in measured propagation constant, the analytical model can be relied upon to infer test specimen impedance changes when significant two-dimensional flow effects are involved.

A math model sensitivity analysis revealed a wide ranging sensitivity of the grazing-incidence impedance to relatively small changes in the absolute slopes of the axial attenuation and phase profiles (the propagation constant components) over the test frequency range. The greatest sensitivity was associated with those frequencies near the antiresonance of the test specimen channels. Most of the propagation constant variability was attributed to the technique for extracting propagation constant components from the measured attenuation and phase profiles.

Symbols

A, B	square matrices
c	sound speed
d_c	diameter of individual test specimen channel
d_s	diameter of sample of test specimen
$F(y,z)$	acoustic pressure eigenfunction
H	duct height (fig. 1)
i	$=\sqrt{-1}$
k	$=\omega/c$, free-space wave number
k_x	dimensional axial propagation constant
$\widetilde{k_x}$	$=k_x/k$, dimensionless axial propagation constant
L	duct width (fig. 1)
l	individual test specimen channel depth
$M(y,z)$	mean-flow Mach number profile
$M_{C/L}$	centerline Mach number
NY, NZ	number of finite elements in y- and z-directions, respectively
$P(x,y,z,t)$	acoustic pressure
Pr	Prandtl number
p_s	static pressure
p_t	total pressure

t	dimensional time
W	normalized characteristic impedance of individual test specimen channel
x, y, z	Cartesian coordinates (fig. 1)
β	acoustic admittance normalized by ρc
Γ	propagation constant of individual test specimen channel
γ	specific heat ratio
δ	incremental change
ς	acoustic impedance normalized by ρc
θ	acoustic resistance normalized by ρc
λ	wavelength
μ	coefficient of viscosity
ρ	density
$\boldsymbol{\phi}$	vector consisting of nodal values of pressure eigenfunctions
χ	acoustic reactance normalized by ρc
ω	angular frequency

Abbreviations:

LE	leading edge of test specimen
SPL	sound pressure level
SWR	standing wave ratio
TE	trailing edge of test specimen

Introduction

The prediction of acoustic attenuation in lined ducts has been of interest for at least 50 years. One of the first attempts to predict duct liner performance was made by Sivian in 1937 (see ref. 1). He obtained measured values of liner impedance and used transmission line theory to predict the propagation constant for plane waves propagating in a circular duct lined with rock wool. Over the past 20 years an urgent need for more efficient acoustic treatments in aircraft engine ducts has produced an abundance of research papers directed toward understanding the fundamental mechanisms of sound attenuation in ducts carrying high subsonic flow and multiple high-order acoustic modes (see, for example, refs. 2–5). This effort has provided a good understanding of the propagation process associated with aircraft engine ducts.

A critical input for all duct propagation models is the liner impedance boundary condition. From a practical standpoint in operational aircraft, the desired impedance must be incorporated into a structure that does not compromise aircraft safety or aerodynamic performance. In practice, these constraints have restricted liner configurations to lumped element resonating systems whose resistive components are implemented by thin porous sheets bonded to honeycomb cores to furnish reactive components as described in references 2 and 3. Thus, there has been an ongoing need to provide accurate determinations of the "effective" impedances presented by such liner configurations in typical aeroacoustic operating environments.

The effective impedance of a duct liner beneath a boundary layer usually depends upon both the intrinsic impedance of the liner and its interaction with the local aeroacoustic environment. The understanding of this interaction has also been the subject of intensive research. For example, there have been numerous experimental and theoretical studies conducted to improve impedance prediction models of the simple perforate and honeycomb core resonators (see refs. 6–12). The proliferation of various prediction models can, in part, be attributed to a lack of accuracy in propagation models (which permit impedance to be "backed out") and in pressure measurements, especially at high mean-flow speeds.

To achieve the full potential of optimally designed liners, it may be necessary to hold the impedance fairly close to an optimum value. For example, in reference 13, Lester and Posey calculated contour plots of constant transmission loss in a fairly large region of the admittance plane for two normalized frequency values. When converted into the impedance plane, a random departure of 0.05 in the normalized impedance components from the optimum value of $0.38 + i0.32$ resulted in degradation up to 7.8 dB in the optimum transmission loss of 49.8 dB. General statements regarding experimental scatter in impedance data are difficult to make. Data reviewed in reference 5 for an installed liner show standard deviations in the normalized resistance of nearly 40 percent for a nominal measured value of 1.0. The data were taken for no flow using a two-microphone method. Melling (ref. 6) obtained careful measurements using the standing wave method on several perforates with honeycomb backed cavities. The scatter in his data ranged from 1 percent in either impedance component to 5 percent and 10 percent in resistance and reactance, respectively, apparently depending on the particular backing cavity depth. Typically, the higher quality measurements reported in the literature exhibit absolute scatter of 0.05 to 0.10 in the normalized resistance for values above about 0.5. Also, the scatter tends to increase with frequency above about 2.0 kHz. Thus, from an optimal design standpoint, the improvement of impedance prediction models and their application to measurement techniques continue to be important.

Measurement of the impedance of an absorbing surface beneath a boundary layer with well-defined accuracy and precision presents a challenging problem. One of the more extensive initial attempts to measure flow effects on duct liner face sheets was made by Feder and Dean in 1969 (see ref. 14). Their approach has been called the "T-tube" method because it makes use of an impedance tube mounted perpendicularly to a flow duct to measure the change in impedance, from the no-flow side, of a porous sheet set into the wall of a flow duct. A special technique to minimize the effect of flow noise was developed to measure standing wave parameters in the normal-incidence sound field impinging on the no-flow side of the test sample. Feder and Dean used their T-tube arrangement to establish impedance trends for several liner face-sheet materials available at that time. The two main disadvantages of the method were the inability to test an assembled liner sample and the necessity of subtracting a measured radiation impedance presented to the test sample by the flow duct.

Some of the problems with the T-tube method can be alleviated by an *in situ* method of impedance measurement discussed by Melling in reference 6. The method requires that one pressure sensor be mounted flush with the liner surface and a second sensor be mounted at the bottom of the backing cavity. The method provides a determination of the

local impedance experienced by an acoustic wave incident at any angle on the flow side of the test sample surface. However, there are several disadvantages: (1) sensor amplitude and phase calibration must be precise and stable; (2) leakage around the face-sheet sensor must be avoided; (3) the measured impedance value is localized and therefore subject to local contamination effects, especially sensor-induced field distortions; and (4) the installation technique is delicate, tedious, and time consuming. In spite of these disadvantages, several investigators (see refs. 15–17) have evidently developed variations of the method to an acceptable level of reliability. Consequently, it serves as a useful complement to the infinite-wave-guide method, which is the final method to be discussed and is the subject of this paper.

The infinite-wave-guide method extracts the acoustic impedance of a liner test specimen via a duct propagation model by using, as input data, the propagation constant derived from measurements of the axial pressure attenuation and phase rates. This method also assumes propagation of only the lowest order mode. Thus, the ultimate reliability of the method depends upon the accuracy of the propagation model and propagation constant measurements. The method is attractive in that it is nonintrusive and does not generally require precision amplitude and phase calibration. Also, the result is more nearly a global impedance measurement since a larger area of liner contributes to the propagation constant at a particular axial location along the test sample length. Armstrong, Beckemeyer, and Olsen (ref. 18) used the method to measure impedance using both zero and uniform flow models. They also developed an analytical model for one-dimensional shear flow, but no experimental data making use of this model were reported. Probably the most serious disadvantage of the method, from an experimental standpoint, is the contaminating effect of end reflections on propagation constant measurements. However, the effect of end reflections is usually minimal for impedance values of interest and can usually be handled by appropriate data processing. Also, severe material nonlinearity essentially invalidates the impedance concept in the context of this method since the impedance becomes dependent on the SPL.

The most practical flow duct geometry for implementing the wave-guide method allows maximum flow Mach number for a given mass flow, isolates the lowest order mode propagation over the frequency range of interest, and permits the testing of flat test specimens of sufficient size to represent parent material average properties. To minimize the mass flow required to achieve a given flow Mach number and to maximize the upper frequency limit at which only the lowest order mode can be supported in a wave guide, a square cross section is desired for a given cross-sectional area. This preference for a square cross section exacerbates two-dimensional shear-flow effects. However, in principle, these effects can be taken into account by a more sophisticated propagation model.

The evolution of propagation models for application to infinite-wave-guide impedance measurements has started from the zero-flow grazing-incidence condition, progressed to uniform flow models, then to one-dimensional shear-flow models, and finally to a two-dimensional shear-flow model by Watson (ref. 19). The purpose of this paper is to perform a limited validation of the shear-flow model of reference 19 in a flow duct (henceforth called flow impedance tube) with a square cross section. To accomplish this goal, special care was taken to choose a test specimen that was demonstrably locally reacting, whose normal-incidence impedance exhibited no measurable amplitude-dependent nonlinearity, and whose structure suggested that grazing-flow effects should be minimal regardless of the sound propagation direction.

Specifically, the propagation model developed in reference 19 was evaluated by testing its ability to reproduce normal-incidence impedance measurements for a well-understood test specimen in a well-controlled grazing-flow environment. This was done for both downstream and upstream sound propagation over a specified frequency range. In essence, the test specimen was used as a calibration test material to build confidence for applying the propagation model to realistic test specimens that would be expected to exhibit changes in impedance due to flow effects. To ascertain the quality of the comparisons, precision and accuracy of both normal-incidence and grazing-incidence impedance data due to random and systematic errors were investigated in some detail.

Analysis

Propagation Model

In this section the boundary value problem which must be solved to determine the impedance of a test specimen installed on one wall of the grazing-flow impedance tube is presented. A more complete development of the two-dimensional shear-flow model employed here is given in reference 19. Assumptions underlying the model development include the small-amplitude assumption for all acoustic quantities relative to the mean values. The acoustic medium is assumed inviscid, non-heat-conducting, and of uniform temperature.

Figure 1 depicts the applicable geometry of the flow duct system and the coordinate system employed in the model. For convenience in the analysis, the upper wall and two sidewalls of the duct are rigid and the test specimen is located along the bottom wall. All four walls are assumed to be of infinite extent in the axial direction (infinite wave guide) and sound waves are assumed to propagate only in the axial direction (i.e., the test specimen length is effectively infinite). The orientation of the coordinate system is chosen as shown in the figure. The mean-flow profiles in the y- and z-directions are assumed to be invariant with respect to the axial coordinate over the extent of the test specimen. Also, it is more convenient in theoretical developments to work with the normalized specific acoustic admittance β. However, in laboratory work, it is general practice to express results in terms of normalized acoustic impedance, $\varsigma = 1/\beta$. The latter practice is followed in this paper.

The solution to the wave equation for harmonic time dependence in the presence of shear flow can be written in the form,

$$P(x, y, z, t) = F(y, z) \exp[-i(k_x x - \omega t)] \qquad (1)$$

where k_x is the axial propagation constant. The following elliptic partial differential equation for the pressure eigenfunction $F(y, z)$ is obtained (see ref. 20):

$$F_{yy} + F_{zz} + \left(\frac{2\widetilde{k_x}}{1 - M\widetilde{k_x}}\right)(M_y F_y + M_z F_z) + k^2\left[\left(1 - M\widetilde{k_x}\right)^2 \widetilde{k_x}^2\right] F = 0 \qquad (2)$$

where the subscripts y and z indicate partial differentiation with respect to y and z. The function $M(y, z)$ specifies the mean-flow Mach number profile, $\widetilde{k_x} = k_x/k$ is the dimensionless axial propagation constant, and k is the free-space wave number (ω/c).

The physical boundary conditions associated with equation (2) require continuity of particle displacement along the wall boundaries (see refs. 3 and 5). These boundary conditions are expressed in the following form for the three rigid boundaries:

$$F_z(y, 0) = F_z(y, L) = 0 \qquad (3)$$

$$F_y(H, z) = 0 \qquad (4)$$

Thus, the normal derivative of the pressure function must vanish along the rigid boundaries. However, for the wall containing the test specimen, this boundary condition is expressed in the form

$$F_y(0, z) = ik\beta\left[1 - \widetilde{k_x} M(0, z)\right]^2 F(0, z) \qquad (5)$$

in which β is the normalized specific acoustic admittance of the test specimen and is to be determined. Note that realistic mean-flow profiles satisfy the condition of no slip at the boundaries, rendering zero mean flow there. In this paper, some unrealistic slip-flow velocity profiles for which $M(0, z) \neq 0$ are also considered. Therefore, the more general boundary condition given by equation (5) is used.

Equations (2) through (5) constitute a boundary value problem for the acoustic pressure eigenfunction $F(y, z)$ and the unknown acoustic admittance β. The solution to this boundary value problem can be cast in terms of known functions only for some special cases of two-dimensional shear flow. However, these cases cannot generally be achieved in the laboratory and are of no use for general application. Further, since the differential equation and boundary conditions are homogeneous, the pressure eigenfunction and acoustic admittance satisfying these equations constitute an eigenvalue problem which must be solved numerically. The solution procedure is as follows (ref. 19): (1) Divide the cross-sectional area of the impedance tube into (NZ $\times$ NY) evenly spaced elements as shown in figure 2; (2) apply Galerkin's weighted residual method to minimize the field error (linear basis functions are used to approximate $F(y, z)$ and $M(y, z)$); (3) account for the effects of the boundary conditions by integrating second derivative terms in the field error by parts and substituting the boundary conditions. This procedure results in a set of linear matrix equations in the form

$$\mathbf{A}\boldsymbol{\phi} = \beta\mathbf{B}\boldsymbol{\phi} \qquad (6)$$

In equation (6), $\mathbf{A}$ and $\mathbf{B}$ are both square matrices of order (NY + 1) $\times$ (NZ + 1) and $\boldsymbol{\phi}$ is a vector consisting of the values of $F(y, z)$ at the various nodes of the system (see fig. 2).

Equation (6) has the form of a generalized eigenvalue problem. Here, the unknown admittance β is the eigenvalue and is determined by the determinant condition:

$$\det(\mathbf{A} - \beta\mathbf{B}) = 0 \qquad (7)$$

in which the notation det denotes the determinant of the matrix. Some further comments concerning equation (7) should be made in order to avoid confusion. First, the solution to equation (6) has been obtained using a special form of the LZ algorithm

(ref. 19), which takes advantage of the banded nature of the matrices in this equation. Currently, matrices on the order of 6000 are easily handled by the algorithm. Secondly, there are a discrete set of eigenvalues β and a corresponding set of pressure eigenfunctions ϕ which satisfy equations (6) and (7). This appears to be contrary to the physics of the problem, for which only a single value of the admittance β exists. The admittance for the physical problem is extracted as follows: (1) The pressure eigenfunction is measured at the centerline ($y = H/2$) of the impedance tube; (2) the admittance value whose pressure eigenfunction gives the best fit to the measured data is determined to be the correct admittance for the physical problem.

Test Specimen Math Model

The test specimen consisted of a distribution of equal-length cylindrical channels embedded in a solid ceramic matrix as depicted in the sketch of figure 3 and the frontal view photograph of figure 4. The photograph shows a sketch of a 6 mm × 10 mm section of the test specimen enlarged by a factor of approximately 10. In the installed configuration (to be discussed in more detail in the section on experimental setup), each channel was considered terminated by a perfectly reflecting surface and acoustically isolated from its neighbors.

Acoustic dissipation (i.e., the resistive impedance component) was assumed to be due mainly to viscous dissipation along the length of the channels as illustrated by the axial particle velocity profile in the top sketch at the right of figure 3. Over the range of test frequencies of interest in this investigation, two longitudinal resonances and one antiresonance existed, as depicted in the remaining three sketches showing axial particle velocity envelopes.

According to Zwikker and Kosten (ref. 21), the impedance at the entrance to a channel of diameter d_c with a perfectly reflecting termination at depth l is given by

$$\varsigma = W\coth(\Gamma l) \tag{8}$$

where Γ is the complex propagation constant in the channel, W is the normalized characteristic impedance (complex) in the channel, and coth denotes the hyperbolic cotangent function. In reference 22, Tijdeman has summarized much of the classical work done on propagation of sound in tubes. In this summary he shows that the various analytical solutions for the propagation constant can be rewritten in terms of a shear wave number. For the purposes of this investigation, the Kirchoff ("wide-tube") solution for the propagation constant (which includes thermal dissipation effects) was found to suffice over the frequency range of interest. In terms of the shear wave number s, this solution is given by

$$\begin{aligned}\Gamma &= \Gamma_1 + i\Gamma_2 \\ &= k\left\{\frac{1}{\sqrt{2}}\left(\frac{\gamma - 1 + \sigma}{\sigma s}\right)\right. \\ &\quad \left. + i\left[1 + \frac{1}{\sqrt{2}}\left(\frac{\gamma - 1 + \sigma}{\sigma s}\right)\right]\right\}\end{aligned} \tag{9}$$

where

$$\left.\begin{aligned} s &= r(d_c/2)\sqrt{\rho\omega/\mu} \\ \sigma &= \sqrt{Pr} \\ W &= ik/\Gamma \end{aligned}\right\} \tag{10}$$

and the subscripts 1 and 2 denote real and imaginary terms, respectively. The average impedance of the test specimen surface is computed by summing the admittances of a representative number of channels to get the total equivalent admittance. If there are N channels and all are identical, this reduces to

$$\beta = \frac{1}{W}\left(\frac{d_c}{d_s}\right)^2 \frac{N}{\coth(\Gamma l)} \tag{11}$$

or the equivalent normalized specific impedance is given by

$$\varsigma = \frac{ik}{N\Gamma}\left(\frac{d_s}{d_c}\right)^2 \coth(\Gamma l) \tag{12}$$

where d_s denotes the diameter of the sample area under consideration (see magnified insert in fig. 4), and d_c represents a typical channel diameter. This result qualitatively describes the measured normal-incidence impedance at the test specimen surface and will be used to provide physical insight for understanding the sensitivity of measured impedance values to measurement error.

Error Analysis

The effects of both random and systematic errors on the normal-incidence impedance, as measured by the standing wave method, were estimated. For grazing-incidence measurements obtained by the infinite-wave-guide method, only the propagation of systematic errors was considered. The analytical treatment for estimating the effect of random errors was that developed by Parrott and Smith in reference 23. In reference 23, probability density functions for standing wave ratios (SWR) and null positions for three different test specimens, covering a normalized impedance range of 0.1 to 20 for resistance and −5 to +5 for reactance, were measured repeatedly until statistically significant samples were

collected. It was shown that measurements of reflection factors and null locations were distributed in a Gaussian manner about their respective mean values with standard deviations of approximately 0.001 for the reflection factor and 1 mm for the null locations. It should be noted that an error of ±0.001 in the reflection factor corresponds to an error of ±0.05 dB in a SWR of 20 dB and to an error of about ±0.5 dB in a SWR of 40 dB. The same experimental setup was used for the normal-incidence measurements which are discussed in this investigation, but with the addition of automatic data acquisition. Therefore, in the normal-incidence measurements reported in this paper, the distribution of random measurement errors was assumed to be the same as that reported in reference 23.

The sensitivity of normal-incidence impedance to systematic errors in the primary measured quantities—SWR and null location—was studied. This was accomplished by assuming that all systematic errors, from whatever source, could be stated in terms of changes in SWR and null location. Maximum error bands for a particular normal-incidence impedance value were computed by mapping the region in the measurement plane defined by "equivalent" systematic errors associated with SWR and null location into the corresponding region of the impedance plane. This procedure does not quantify the absolute magnitude of the systematic error. It does, however, provide some insight as to which regions of the measurement plane are critical with respect to systematic measurement error.

Similarly, the sensitivity of grazing-incidence impedance to systematic errors in the primary measured quantities—axial attenuation and phase rate (from which the propagation constant is derived)—was studied. It was assumed that all systematic errors could be stated in terms of changes in sound pressure and phase relative to the test specimen leading edge. Again, maximum error bands for a particular grazing-incidence impedance value were computed by mapping the region defined by "equivalent" systematic errors associated with a measured value of propagation constant into the corresponding region of the impedance plane. Again, this procedure does not quantify the absolute magnitude of the systematic error, but it does provide some insight as to which regions of the propagation constant plane are critical with respect to systematic measurement error. Sensitivity to grazing-flow variation about nominal measured values was not examined analytically, since the test specimen in this investigation was specifically chosen to exhibit minimal effects of grazing flow.

Propagation constant measurements reduce to the determination of the slopes of the axial attenuation and phase profiles corresponding to single mode propagation over the test specimen surface. The simplest way to extract the slopes is via a linear least-square fit to the "approximately linear region" of the profiles. It is of interest to relate systematic changes in the individual measurements of sound pressure level and phase to resulting changes in the slopes. If N is the total number of data point pairs (X_i, Y_i), then from standard textbooks, the slope of the linear least-square fit is

$$a_2 = \frac{N\sum_{i=1}^{N} X_i Y_i - \sum_{i=1}^{N} X_i \sum_{i=1}^{N} Y_i}{N\sum_{i=1}^{N} X_i^2 - \sum_{i=1}^{N} X_i \sum_{i=1}^{N} X_i} \tag{13}$$

Define

$$A = \sum_{i=1}^{N} X_i^2 \quad B = \sum_{i=1}^{N} X_i$$

$$D = NA - B^2$$

Then equation (13) can be rearranged to become

$$a_2 = \frac{1}{D}\sum_{i=1}^{N} (NX_i - B)Y_i \tag{14}$$

The average value of the X_i coordinates is

$$\overline{B} = \frac{B}{N}$$

and if small systematic changes ϵ_i are assumed in Y_i, then the resulting change in the slope a_2 is

$$\delta a_2 = \frac{N}{D}\sum_{i=1}^{N} (X_i - \overline{B})\epsilon_i \tag{15}$$

As is intuitively clear from geometrical considerations, changes in the slope are more sensitive to changes in the Y_i toward the extremes of the data fit since the quantity $(X_i - \overline{B})$ decreases as X_i approaches $\overline{B}$.

To determine the effects of random measurement error on propagation constant measurements, it is also of interest to relate the variances in the individual measurements of sound pressure level and phase to the variances in the slope of the linear least-square fits to these data. As shown in reference 23, random error in the slope of a linear least-square fit due to random error in the data can be easily calculated if the variances $\sigma^2(Y_i)$ are equal, that is,

$\sigma^2(Y_i) = \sigma^2(Y_{i+1})$. The variance in the slope of the least-square fit due to variances $\sigma^2(Y_i)$ is then given by

$$\sigma^2(a_2) = \sigma^2(Y_i)\left(\frac{N}{D}\right) \tag{16}$$

Typically, the ratio N/D becomes small as N becomes large; thus, the variance in the slope becomes a small fraction of the data variance if a sufficient number of data points are taken.

Experimental Setup, Evaluation, and Test Procedure

Flow Impedance Tube Apparatus Description

The wave-guide method for measuring the impedance of an absorbing surface beneath a boundary layer was implemented in the flow impedance tube apparatus (FIT) at the Langley Research Center (ref. 24). This multi-configurational apparatus is designed to produce a controlled aeroacoustic environment with a sound pressure level of up to 140 dB and a flow speed of up to Mach 0.6 over a test specimen length up to 40 cm. In the standard configuration, sound propagates downstream with the flow; however, upstream propagation can be achieved by relocating the driver downstream of the trailing edge of the test specimen. The overall layout of the facility is depicted schematically in figure 5.

Moving from left to right in figure 5, the apparatus can be divided into three sections as indicated. The source section begins with a supply plenum from which air percolates into a round, 5.7-cm-diameter duct constructed of high resistance fiber metal. For downstream propagation, an acoustic driver is attached at the upstream end as indicated. A thermocouple located at the plenum exit provided a control point for airflow temperature, and a pitot-static tube located about 12 duct diameters downstream from the plenum exit provided a means for determining the reference centerline Mach number. To gain stability, the airflow rate and temperature were controlled to set points by electro-pneumatic regulator valves and electric heaters connected to a 150-psi supply line.

The flow moves into the test section of the apparatus through a round to square, constant-area transition (not shown). The test section accommodates the test liner specimen, the axial traverse bar, and various transducers, of which only the traverse-bar-mounted probe microphone is indicated. Other transducers are described in greater detail with the schematic of figure 6. The end purpose of the apparatus is to generate axial attenuation and phase rate data so that the propagation constant for the fundamental propagation mode over the test specimen can be extracted. An illustrative format for such data is shown in figure 5 beneath the test liner specimen.

Downstream from the exit of the test section, the flow and sound are absorbed by a termination designed to minimize acoustic reflections and flow noise. Also, just upstream of the termination entrance, an adapter plug was included to allow installation of the acoustic driver when upstream propagation was desired. The termination section consisted of a square-cross-section duct with two opposite sides lined with open cell foam contained in 30-percent-open perforate U-shaped channels. The foam was mechanically compressed in the U-shaped channels so that the density varied by an approximate 10:1 ratio from the upstream to the downstream end. The airflow was removed in a gradual manner along the entire length by inducing a pressure gradient across the foam lining via a vacuum line as indicated in the sketch. This arrangement provided a quiet exit for the flow and minimized acoustic reflections. Reflection factors were not greater than 0.06, or equivalently, the standing wave ratios were not greater than 1 dB from 0.5 kHz to 3.0 kHz both with and without flow.

The part of the test section accommodating the test liner specimen is depicted in figure 6. This sketch shows additional instrumentation used in this investigation. In addition to the probe microphone, the traversing bar carried a vertically traversing total pressure rake and a static pressure port to ascertain changes in vertical flow profiles along the test specimen. Also, in the sidewall midway along the axial span of the test specimen, provision was made for the interchangeable installation of a probe microphone or a horizontally traversing total pressure rake to examine horizontal acoustic pressure distributions and flow profiles. Fixed microphones were flush mounted in the sidewall at the leading and trailing edges of the test specimen to monitor overall transmission losses. Finally, a temperature sensor was installed flush with the bottom inside wall surface a short distance upstream of the test specimen leading edge.

A block diagram of the electronic instrumentation necessary for measuring mean-flow characteristics is shown in figure 7. Total and static pressures at the reference location (see fig. 5) were measured by electronic manometers as were the test section total and static pressures. Eight total pressures associated with the eight-tube pressure rake were measured with a single manometer in conjunction with a computer-controlled scanning valve. All pressures were multiplexed into a digital voltmeter and stored for later processing. The manometers also provided direct digital readouts for on-line monitoring.

The automatic flow control system was designed to maintain set points of total pressure p_t and static pressure p_s at the reference location (see fig. 5) to within system-dependent error bounds. This was accomplished automatically by continuous adjustment of the supply pressure and vacuum. The system was capable of maintaining "long term" variations about target values to within about ±3 mm Hg. These small changes in total and static pressure, over time periods of 5–10 minutes, and the relatively slow response times of scanning valve and pressure sensor units necessitated four pressure measurements for each rake tube (static and total for reference location and the same for a particular rake tube) to ensure the measurement of an "instantaneous" velocity profile. This procedure allowed the time and spatial variance of the flow profiles over the test specimen to be evaluated. Essentially, changes in total and static pressures at the reference location were measured after each measurement of the corresponding quantities for a particular rake tube. The rake tube total and static pressure were then corrected by the change at the reference location since the start of the test. In this manner the flow profile for each rake tube could be related to the same nominal Mach number at the reference location.

The flow profile data $M(y, z)$ were conditioned for input to the grazing-incidence impedance math model (eq. (2)) by curve fitting. In the viscous sublayer, a linear extrapolation to zero velocity at the test specimen boundary was used. A 1/7 power law was then applied in the region that exhibited turbulent boundary layer behavior, and a polynomial curve fit was used for the remainder of the flow profile. Continuity of slope was required at the curve transition points.

Acoustic instrumentation consisted of flush-mounted microphones, an acoustic pressure probe, and an acoustic driver as depicted in figures 5 and 6. The pressure probe was constructed by bonding a strain-gage-type pressure sensor into a 3-mm-diameter probe described in detail in reference 25. The flush-mounted transducers were 6-mm-diameter condenser-type microphones. An electrodynamic 120-watt driver was used to generate discrete frequency acoustic waves for both downstream and upstream propagation at sound pressure levels such that acoustic data could be collected over a dynamic range of at least 50 dB.

The conditioning instrumentation and data processing system for the acoustic signals are shown schematically in figure 8. For a given test frequency and flow Mach number, a preselected sound pressure level was set at the leading edge of the test specimen via the computer-controlled frequency synthesizer. Acoustic pressure and phase were then obtained at uniformly spaced locations in the axial direction along the centerline of the test section. Because of high flow noise levels, the signal was prefiltered with a 50-Hz-band-pass filter and then subjected to synchronous ensemble averaging to further reduce flow noise contamination. Final processing of the signal was done by an on-line sine wave curve-fitting routine to obtain the amplitude and phase of the component at the excitation frequency. From such information, gathered over the length of the liner's linear decay region, the propagation constant was obtained.

Test Environment Evaluation

As mentioned previously, the automatic flow control system was able to control static and total pressures at the reference location to within ±3 mm Hg of the set point. In fact, these variations were highly correlated. A worst case sample of total and static pressure variations over a 3-hour period and for a nominal centerline Mach number of 0.1 is shown in figure 9. Because of the correlated variations of total and static pressure, the resulting variation in Mach number was not more than 3 percent.

Figure 10 shows the extrema of static and total pressures versus distance along the test section for a nominal centerline Mach number of 0.3. The relative location of the test specimen is shown by the rectangular hatched region starting at the origin of the x-coordinate. Pressures are stated in mm Hg relative to ambient atmospheric pressure. Open triangular symbols represent maxima and minima in the total pressure as indicated in the figure key. Static pressure maxima and minima are represented by shaded symbols. These measurements were taken during the extrema of total and static pressure variations observed over a continuous time period, as illustrated in figure 9. The solid line represents the theoretical pressure drop with distance for turbulent flow through a circular duct of equal cross-sectional area. Clearly, the data suggest an approach to fully turbulent flow over the test specimen region.

Velocity profiles were measured at the test section center axial location ($x = 20$ cm) in the absence of a test specimen to further investigate flow symmetry and stability. Representative examples of vertical profiles at $z = 1.91$ cm are shown in figure 11 for the three Mach numbers of interest in this investigation. The lower wall surface is located at $y = 0$ and the upper wall is located at $y = 5.08$ cm. As expected, the profiles are seen to change shape with increasing Mach number. Most of the apparent asymmetry near the walls is associated with measurement point placement asymmetry. Similar results were obtained

for profiles measured in the horizontal direction (i.e., along the z-axis at $y = 2.54$ cm).

To further ensure stable flow conditions during tests, the temperature of the flow, as measured by the thermocouple at the plenum exit, was set equal to the average ambient temperature. This was accomplished by means of the temperature sensor installed upstream of the test specimen location as indicated in figure 6. This information was used to adjust the set point for airflow temperature control via the thermocouple located in the airflow at the plenum exit. Ambient temperature variations and control system error bounds allowed the test section wall temperature and the total temperature of the flow to be maintained to within about 2°C.

Test Mach numbers of 0.1, 0.3, and 0.5, as measured on the centerline at the reference location, were used in this investigation. The minimum of 0.1 was chosen because data scatter in the total static pressure measurements became excessive at smaller values. The maximum of 0.5 was chosen because it was the highest value that could be consistently attained.

Test Specimen

As discussed under "Analysis," the test specimen consisted of a ceramic honeycomb structure which had a porosity (open area ratio) of 0.57 and was permeated with parallel cylindrical channels with diameters of about 0.64 mm and lengths of 8.25 cm (shown in fig. 3). The material was machined and fitted to a test specimen fixture as illustrated in the photograph of figure 4. The machined surface perpendicular to the channel axes was sensibly smooth. Normal-incidence impedance was measured prior to the present tests using the transmission line method at four locations along the test specimen surface and at 100-Hz frequency increments. These measurements are reported in reference 26 and reproduced here to establish a baseline for evaluating the grazing-incidence, grazing-flow impedance measurements on the same specimen.

The normal-incidence impedance data are presented in figure 12 along with the math model prediction from equations (8) and (9). Table I presents the same data in tabulated form along with the average values for the four specimen locations, which are represented by the solid curve in figure 12. The table also presents calculated absolute and relative variability of the data as defined in the table headings. Absolute variability is seen to range from about 0.02 to 0.20 for the resistance and 0.01 to 0.29 for the reactance. Relative resistance variability ranges between 0.03 and 0.11. On the other hand, relative variability of the reactance is meaningless because of the zero crossings. Therefore, absolute variability is the focus of attention in this work. Both the absolute variability and the calculated systematic error bound extrema, as indicated by the error bound symbol in figure 12, correlate approximately with the rate of change of the impedance with frequency. The random error contribution (short dashed line in fig. 12) was based on the results of reference 23 and is derived from standard deviations in the reflection factor and null location of 0.003 and 0.3 mm, respectively. Note that the standard deviations associated with random error have been scaled up by a factor of 5 for plotting purposes.

To aid in discussing the quality of the impedance data, it is appropriate to define the role of systematic and random fluctuations in the measurement process. For the purpose of this investigation, fluctuations are classified as due to random measurement error if they arise from a statistically significant number of repetitive measurements of a readily identifiable quantity of primary relevance to the measurement process (e.g., sound pressure level, standing wave ratio, null position, or phase). Fluctuations will be classified as systematic if the fluctuation interval tends to be long relative to that of a typical test run and if they are somewhat vaguely identified with the test conditions, for example, test specimen mounting conditions, ambient temperature, or instrumentation drift. As explained in reference 23, systematic errors associated with primary measurement quantities propagate with their algebraic sign intact, whereas random errors do not. Thus, it will be convenient to lump all systematic errors into "equivalent" systematic errors in the measured acoustic quantities of primary relevance to the particular measurement process of interest.

As reported in reference 23, and confirmed again for the data of figure 12 (taken for a different test specimen), random measurement errors do not explain the observed variability. On the other hand, the trends in the systematic error bounds calculated from assumed equivalent systematic errors of 0.1 dB and 0.1 mm in SWR and null location, respectively, are seen to be consistent with the data variability. The results of reference 23 suggest that systematic errors probably arise from mounting condition variability, instrumentation calibration drift, and uncontrolled changes in the test environment, as opposed to direct systematic errors in SWR and null location measurement.

When interpreted as equivalent systematic error, SWR and null location errors as low as 0.1 dB and 0.1 mm, respectively, are probably as small as can be expected with present measurement techniques. The importance of mounting conditions and surface inhomogeneities to the increased data variability in

the vicinity of the antiresonance at 1.9 kHz can be further appreciated by examining the math model for the test specimen (eqs. (8) and (9)) in the limit as the propagation constant Γ becomes purely imaginary (i.e., no attenuation along the channel wall). This condition causes the $\coth(\Gamma l)$ behavior to degenerate into $-i\cot(kl)$. Resonant liners consisting of honeycomb backed porous face sheets are typically modeled in the literature (see ref. 3) by an equation of the form

$$\varsigma = \theta_f \left(1 + i\frac{\omega}{\omega_c}\right) - i\cot\left(\frac{\omega}{\omega_c} l\right)$$

where θ_f and ω_c are the liner face-sheet flow resistance and characteristic frequency, respectively. In many cases (ω/ω_c) is small enough to be neglected so that

$$\varsigma = \theta_f - i\cot(kl)$$

When the impedance of such a lumped-element resonant liner is measured over a range of frequencies that includes an antiresonance of the backing cavity (i.e., cavity depth equal to one-half the acoustic wavelength), a strong spike is observed in an otherwise nearly constant resistance (see ref. 23). Much variability in the measured resistance is observed in the vicinity of antiresonance frequencies. It appears from figure 12 that a similar, but less dramatic, trend is evident in the ceramic honeycomb test specimen, which has the resistance distributed over the length of the cavity. In this case, however, the effect of the antiresonance at 1.9 kHz is evident over a bandwidth of at least 1.0 kHz centered at the antiresonance frequency. Such a resonant absorber with distributed resistance offers a good opportunity to test impedance measurement methods in the vicinity of both resonance and antiresonance frequencies. This is important because, depending on the magnitude and the means by which resistance is incorporated into a resonant absorber system, antiresonance effects may be significant over large bandwidths.

This particular test specimen was chosen because it was anticipated that the ceramic honeycomb structure would exhibit a high degree of acoustic linearity, local reaction, and little effect of grazing flow on the impedance. Locally reacting behavior was enhanced by the rigid ceramic matrix and by sealing the channel terminations. The channel length-to-diameter ratio of 128 (see fig. 3) and large open area ratio of 0.57 suggest that most of the resistive component is furnished by dissipative processes distributed thoughout the channel length. This is in contrast to typical, lumped-element-type liner constructions in which the resistive element is concentrated in the vicinity of the face sheet. Therefore, grazing flow has much less capability of altering the resistance of the ceramic honeycomb structure. The same rationale holds for the reactive component with the exception of small values of reactance (i.e., near resonance).

Results and Discussion

Flow Profile Data

The motivation for complicating the grazing-incidence impedance math model by introducing shear flow is to include the potential effects of nonzero boundary layer thickness and acoustic refraction on the test specimen effective impedance. These effects can be handled approximately by a one-dimensional shear-flow model if the rectangular cross section of the flow impedance tube has a sufficiently large aspect ratio. As discussed previously in the "Introduction," design considerations for a flow impedance tube suggest a square cross section for maximum flow speeds, test frequencies, and optimal test specimen geometry. Thus, the trade-off for more flexibility in the experimental test facility is a more complex math model for inferring the grazing-incidence impedance.

The math model under discussion here assumes the mean-flow velocity profiles to be invariant with respect to axial distance over the test specimen length. It is of interest therefore to determine the degree to which this assumption is satisfied with the test specimen installed in the flow impedance tube. Figures 13(a) and 13(b) show plots of eight superimposed vertical velocity profiles at the leading edge ($x = 0$) and trailing edge ($x = 39.4$ cm), respectively, of the test specimen. The nominal centerline Mach number is about 0.27 in the test section for a centerline Mach number of 0.3 at the reference location (see fig. 5). For each of eight locations along the z-axis, the Mach number is plotted versus vertical distance y from the test specimen surface. Note that the second column in the keys of figure 13 gives the z-coordinates normalized by the test section, or specimen width. Thus, the profile measurement positions on the z-axis ranged from 14 to 98 percent of the test section width.

Comparison of figures 13(a) and 13(b) shows that with the exception of the rake element located at $z = 5.00$ cm (i.e., within 0.76 mm of the wall), the profiles show little variability over the length of the test specimen. In particular, little change in profile slopes (i.e., M_y) was observed near the test specimen surface either in the x- or z-directions. Horizontal velocity profiles were measured using a similar rake assembly at the midspan of the test specimen ($x = 20$ cm). These measurements exhibited

the same general character as the vertical profiles of figure 13(a). In view of these observations, all mean-flow velocity profile data used as input to the shear-flow math models were obtained at the midspan location of the test specimen and were considered representative of the flow profile character over the entire axial span of the test specimen.

Acoustic Measurements

It was desirable to validate the shear-flow analytical model for measuring grazing-incidence impedance at a number of test frequencies so that both high and low attenuations would be represented. To determine these frequencies, the insertion loss of the test specimen was determined using broadband acoustic excitation in the absence of flow. For the data of figure 14, tape was placed over the last 5.1 cm of the test specimen to allow pressure measurements to be made downstream of the "'effective" trailing edge. The hard wall sound pressure levels (i.e., no specimen in place), as indicated by the dashed curve, were measured by a flush-mounted microphone located about 5.1 cm beyond the trailing edge of the test specimen. The solid line shows the sound pressure levels at the same position with the test specimen installed. Clearly, maximum insertion losses occur near 0.9 kHz and 2.6 kHz. The dashed vertical lines in the figure indicate the test frequencies chosen for this investigation.

Estimation of the propagation constant for a given test condition is the most critical aspect of the infinite-wave-guide impedance measurement method. This is accomplished by determining axial attenuation and phase rates for a single propagating mode. Figures 15(a) and 15(b) illustrate typical axial attenuation and phase profiles, respectively, at 0.8 kHz and for three flow conditions along a reduced length of the test specimen. This was done to show the test specimen attenuation and phase profiles in context with the effects of end reflections. The reduced length was obtained by covering a 10-cm length at the trailing edge of the specimen with tape, as indicated by the dashed line in the photograph of figure 4. The vertical dashed lines in figure 15 indicate the leading edge and "effective" trailing edge of the test specimen for this test. In this figure, attenuation and phase data for nominal Mach numbers of 0.1 and 0.3 at the reference location are compared with those for zero flow. Sound propagates from left to right with the flow. Sound pressure level and phase are referenced to the test specimen leading edge.

For all three test runs shown in figure 15, a nearly linear region is observed to exist over a 10- to 15-cm length of the specimen for both the attenuation and the phase profiles. The most obvious effect of combining flow and sound in the same direction is to decrease the attenuation rate. Also, leading edge reflections cause standing waves of at least 10 dB upstream of the leading edge. Transition to the linear attenuation region occurs within about 5 cm of the leading edge and contaminating effects of trailing edge reflections on the linear attenuation region are barely evident at the highest flow speed of Mach 0.3. Also, the axial phase profiles are less affected by flow than are the axial attenuation profiles. These observations suggest that this particular test specimen should, at least for the selected frequencies, produce well-defined linear attenuation regions for estimating single mode propagation constants.

Determining linear decay rates for attenuation and phase profiles corresponding to a single propagating mode is the central focus of this experimental procedure. This can be done either by a linear least-square fit to the data or by a least square fit of a single mode propagation model that includes end reflection effects. The extraction of propagation constants from data of the kind illustrated in figure 15, but taken over the entire specimen length, is now discussed with attention given to sources of systematic and random errors.

Figures 16 through 21 show a sequence of measured axial attenuation and phase profiles over the entire test specimen length of 39.4 cm for test frequencies of 0.5, 1.0, and 3.0 kHz, for centerline Mach numbers of 0.3 and 0.5, and for downstream sound propagation. These data are representative of those used to infer the test specimen impedance and thereby to evaluate the shear-flow math model of interest in this investigation. The slope of the solid line, which is a linear least-square fit to the data, provides the simplest method for estimating the propagation constant. The intercept, slope, and correlation coefficients are given in the figure keys. Examples of both "low" and "high" quality data are represented in these figures.

Figure 16(a) shows one of the more dramatic examples of the effect of trailing edge reflection. The edge reflection sets up a standing wave pattern as indicated by the dashed curve faired through the data. It was anticipated that the linear least-square fit for these data (solid line in the figure) would not extract the underlying linear attenuation rate with sufficient accuracy. Therefore, the data were also fitted with a least-square single mode wave propagation model. In this fitting procedure, the edge reflection factor, Mach number, and propagation constant components were allowed to vary until fits to the attenuation and phase profiles were optimized. This procedure provided quite reasonable fits to data that exhibited

strong standing wave phenomena. Unfortunately, for data with lower standing wave ratios, this fitting procedure was poor. Thus, improvements to this single mode propagation model could be expected to improve the quality of results.

One possible improvement in this model would be the inclusion of high-order modes. Obviously, this would destroy the simplicity of the infinite-wave-guide method. Also, the inclusion of high-order modes in the fitting procedure was beyond the scope of this investigation because it would require a modal decomposition scheme and extensive additional measurements in the duct cross section.

With few exceptions, the measured sound pressure level attenuation and phase profiles exhibited little or no discernible trailing edge reflection effects. A typical example of such data is shown in figure 17. Figure 18 shows a modest trailing edge reflection effect for one of the higher test frequencies (3.0 kHz). However, at the highest Mach number of 0.5, some unexpected patterns did occur in the attenuation and phase profiles. Two such examples are shown in figures (19) and (20) for frequencies of 0.5 kHz and 1.0 kHz, respectively. In figure 19(a) the faired dashed line through the data suggests a modulated standing wave. Note that the corresponding phase profile of figure 19(b) shows a relatively linear region for the first 23 cm downstream of the leading edge. Figure 20(a) shows an even more irregular attenuation profile pattern and the phase profile of figure 20(b) shows a very large slope of nearly 40°/cm. This large increase seems inconsistent with the more slowly increasing slopes observed at other test frequencies. Finally, figure 21 again shows expected behavior of both the sound pressure level profile and phase profile at a Mach number of 0.5 and at 3.0 kHz, the highest frequency tested.

Some possible causes for the anomalous behavior depicted in figures 19 and 20 are reviewed here. Spatially modulated standing wave patterns can be produced by interaction of the acoustic waves with structure-borne waves in the duct walls or by interaction of two or more acoustic modes. The excitation source of structure-borne waves could be flow turbulence in the air supply valve because significant increases in vibration levels were observed at the highest flow Mach number of 0.5. Another potential source of structure-borne waves is excitation from the driver, which was mechanically coupled to the air supply plenum. This source seems unlikely, however, since modulated attenuation patterns did not occur at the lower flow speeds. A final possibility is the cut-on of a higher order acoustic mode. Transverse pressure measurements in the test section revealed that nonuniform pressure distributions and increased flow speed does lower the cut-on frequencies of the duct. However, this effect should first become evident at the highest test frequency. The occurrence of higher order mode contamination at the lowest test frequency is inconsistent with the observation of "clean" attenuation profiles at the highest test frequencies. In summary, the observed modulation is consistent with acoustic and structure-borne wave interactions. Within the scope of this investigation, the measured attenuation and phase profile behaviors shown in figures 19 and 20 were considered anomalous and, although the extracted propagation constants were generally not discarded, the creditability of the resulting impedance values was discounted. However, for the extreme case at 1.0 kHz and a flow Mach number of 0.5 (fig. 20), the impedance was not computed since the slope of the attenuation profile was not acceptable within the context of the infinite-wave-guide method for measuring grazing-incidence impedance.

Data quality improved and the anomalous behavior discussed above disappeared for upstream sound propagation. Figures 22 through 24 show sound pressure level and phase profiles for flow Mach numbers of 0.3 and 0.5 at test frequencies of 0.5 and 1.0 kHz for upstream propagation. Note that for sound propagating against the flow, the attenuation and phase profiles decrease from right to left. Also, for these profiles, the least-square wave propagation model provided no consistent improvement over the linear least-square method for estimating the propagation constants. Note that barely discernible trailing edge reflections (at $x = 0$ in this case) occurred in the attenuation profiles in figures 22(a) and 24(a). The linearity of the phase profiles for upstream propagation was excellent.

The improved data quality for upstream sound propagation implies that the absorbing efficiency of the section upstream of the leading edge (see fig. 5) need not be as great as that of the section downstream of the trailing edge to avoid potential data contamination by reflections. This is largely a consequence of the more rapid attenuation of upstream propagating sound. Thus, if the direction of sound propagation with respect to flow has no effect on the test specimen impedance, these results suggest that higher quality data are obtained for upstream propagation.

Changes in the measured propagation constants are directly proportional to changes in the slopes of the attenuation and phase profiles. As mentioned previously, almost all the slopes could be accurately extracted from linear least-square fits to the data. The best repeatability attainable for individual SPL

and phase measurements over a time period of about 24 hours with the measurement system used in this experiment was never better than about 0.2 dB and 2°, respectively. This range of repeatability would translate into changes in attenuation and phase profile slopes by about 0.005 dB/cm and 0.05°/cm, respectively. In practice, of course, many factors other than instrumentation drift can contribute to variability in the propagation constant measurements. However, the instrumentation drift limits of 0.2 dB and 2° are used as a baseline to determine the sensitivity of grazing-incidence impedance measurements to systematic variability in the propagation constant.

Variability in the profile slopes due to random measurement errors in sound pressure level and phase can be estimated from equation (16) relating the slope variance to the variance of individual measurements defining the profile. Random measurement errors in the context of this experiment are at least an order of magnitude smaller than the longer term systematic errors discussed in the previous paragraph. Also, the application of equation (16) for $N = 8$, one half the number of data points defining a profile, shows that the slope variance is about 0.4 percent of that of the individual measurements. Therefore, the random measurement error contribution to slope variability is considered insignificant.

Grazing-Incidence Impedance Comparisons

Before proceeding, recall that the purpose of this investigation is to validate the two-dimensional shear-flow math model as developed in reference 19 for inferring grazing-incidence impedance using the infinite-wave-guide method. Ideally, this goal could be accomplished if a linear, homogeneous, locally reacting test specimen were available that exhibited "known" impedance changes due to grazing flow. Unfortunately, such a test specimen is not available. To perform a validation test in a limited way, a test specimen was intentionally chosen to exhibit little or no effect of grazing flow and yet provide a range of impedance values likely to be encountered in practical situations. These results provide a validation of the two-dimensional shear-flow model in the sense that the answer is known, on a physical basis, before the test is conducted. Also, it should be noted that, even though no change in impedance due to grazing flow is expected, all the terms in the math model (i.e., eq. (2)) were exercised in this test.

An appropriate next step in the validation process would be to devise a linear, homogeneous, locally reacting test specimen with known impedance changes due to grazing flow. However, the confidence level in other experimental methods is not such that any single one can be regarded as a standard. Consequently, further validation must necessarily reduce to a comparison of two independent methods such as the infinite-wave-guide versus the *in situ* method.

Figures 25 through 27 show grazing-incidence impedance data, normalized by ρc, for the ceramic honeycomb test specimen. Each of the three figures shows the results of using a progressively more sophisticated flow profile model for "backing out" the grazing-incidence impedance via the finite-element solution of equation (2), with 49 elements in both the y- and the z-direction (NY = NZ = 49). In figure 25, a uniform plug flow profile model was used. An averaged flow Mach number for this model was obtained by an area integration of the two-dimensional flow velocity profile data illustrated in figure 13, that is,

$$M = \frac{\int_0^L \int_0^H M(y,z)\, dy\, dz}{LH}$$

In figure 26, a one-dimensional (1-D) shear-flow profile model was used. In this flow model, the vertical velocity profile located at $z/L = 0.51$ was used to model the entire flow profile, that is, $M = M(y, 0.51L)$. In figure 27, a two-dimensional (2-D) shear-flow profile model was used that included all the vertical flow profile data of the type illustrated in figure 13. If all the measurements were perfect and all the assumptions about the test specimen were ideally satisfied, then all three flow profiles would produce the same result. Thus, the three impedance data sets inferred via the three flow models serve as a consistency test.

Specifically, the three figures compare grazing-incidence impedance data, for four flow conditions, with normal-incidence data. The normal-incidence impedance curve is a reproduction of the averaged impedance shown in figure 12. Normalized resistance and reactance are given in parts (a) and (b) of each figure, respectively, for four flow conditions, with the normal-incidence value included as a baseline in each of the figures. Note that the upper left plot ($M_{c/L} = 0$) is repeated in each figure for reference purposes. The square and round symbols represent results for downstream and upstream sound propagation, respectively. Maximum systematic error bounds (see figure key) were calculated by the procedure discussed in the analysis section. All possible combinations of positive or negative changes in attenuation and phase profile slopes caused by changes in profile slopes of ±0.0025 dB/cm and ±0.025°/cm, respectively, were examined for each test frequency. These particular limits were chosen because they were thought to be the best attainable repeatability

under ideal conditions. They should in no way be interpreted as the repeatability actually obtained. The main purpose for inserting these error bound calculations is to provide an indication of which frequencies are more vulnerable to systematic error.

An inspection of all the figures reveals generally good agreement between grazing-incidence and normal-incidence impedance results. In particular, the agreement between grazing-incidence and normal-incidence data for the no-flow condition is excellent. As might be expected, the agreement tends to degrade when the flow is turned on, but only at specific frequencies and flow conditions. For the uniform flow model (fig. 25), the downstream propagation results remain in good to excellent agreement with the normal-incidence data, whereas the upstream propagation results depart substantially, especially at the highest flow Mach number of 0.5. Most of this departure at Mach 0.5 for upstream propagation occurs at the two highest frequencies of 2.5 and 3.0 kHz and is removed with the use of the shear-flow models as shown in figures 26 and 27. For the most part, the 1-D and 2-D shear-flow models are in good agreement for both downstream and upstream propagation except for the frequencies of 1.5 and 2.0 kHz. These frequencies are in the region dominated by the specimen antiresonance where small systematic errors in the propagation constants can cause relatively large changes in the impedance as indicated by the wide ranging error bounds. In general, these results hold no surprises except that impedances from the upstream propagation data seem to depart further from the normal-incidence impedances than do those from downstream propagation data, whereas the quality of upstream propagation attenuation and phase profiles appears superior to that of the downstream propagation profiles. Table II displays the impedance results as determined using the three computational models (uniform, 1-D shear, and 2-D shear flow) versus the impedances obtained using normal-incidence measurements. Careful examination of the shear-flow results reveals that, in general, the 2-D results are closer to normal-incidence values than the 1-D results. The exceptions to this observation tend to occur at the more sensitive frequencies, such as those near the specimen antiresonance.

It is of interest to note that the error bounds are not generally symmetrical with respect to the data points around which the variations are calculated. This is in contrast to the same procedure used to calculate the systematic error bounds for the normal-incidence data of figure 12 which appear nearly symmetrical with respect to the base point. A careful examination of the numerical results for the normal-incidence error bounds does reveal asymmetry. However, it appears that small systematic errors in the propagation constant have the potential for being much more asymmetrical and of greater consequence than the errors in normal-incidence measurements.

Propagation Constant Variability

Measured propagation constant variability and the resulting effect on grazing-incidence impedance were investigated by repeating attenuation and phase profile measurements over a time period of several days. The reported results are limited to downstream sound propagation at frequencies of 0.5 and 2.0 kHz and for a flow Mach number of 0.3. The frequencies 0.5 and 2.0 kHz were chosen because they exhibit minimum and maximum sensitivity, respectively, to systematic error. Table III displays relative changes between the results of three test cases. The first line for each frequency corresponds to the baseline data already discussed in figures 25 through 27. Moving from left to right across the table, the table entry labeled "Slopes," lists the phase profile and attenuation slopes in deg/cm and dB/cm, respectively. The next entry lists the relative changes in the attenuation and phase profile slopes for the second and third test relative to those of the first test. Finally, the last two table entries list the impedance components and their relative changes.

Several general features of these data are worthy of note. Observe that as the frequency increases from 0.5 to 2.0 kHz, the phase and attenuation profile slopes increase by factors of about 2.5 and 2.0, respectively. The resistance component increases approximately by a factor of 10, while the reactive component remains fairly constant. Relative changes in the phase and attenuation profile slopes for the repeat tests at 0.5 kHz range from 2.5 to 4.9 percent. In contrast to these changes in attenuation and phase profile slopes, the impedance component changes for the repeat tests ranged up to nearly 16 percent for 0.5-kHz data and to almost 62 percent for the 2.0-kHz data. As suggested by the error bound calculations presented in figures 25 through 27, these results confirm that the effects of systematic measurement error strongly depend upon the particular frequency being investigated.

The tests reported in table III were conducted over a time period of 1 day or more during which flow temperature varied by no more than 3°C. Test specimen leading edge sound pressure levels were held constant during a given test to within ±0.2 dB but ranged from 124 to 140 dB for the test series. To maintain maximum dynamic range, driver output

was maintained near its maximum so that no attempt was made to duplicate sound pressure levels from test to test. The repeatability, however, was not observed to significantly improve in those few cases when leading edge sound pressure levels were duplicated. Within these operational limits, the data of table III represent some of the best attainable repeatability for the entire test series.

Direct overlay of repeated attenuation and phase profiles suggested that most of the slope variability arose from the least-square fitting procedure. There was always an element of subjective judgment involving which of the profile data points, if any, to exclude from the "linear" region. As discussed previously, consistency of results was not improved by implementing a single mode least-square fit wave propagation model that permitted the trailing edge reflection factor to systematically vary until a best fit was obtained.

For the reasons presented above, the weakest part of this experimental procedure is most likely the procedure for extracting the propagation constant via the slopes of the attenuation and phase profile measurements. One partial solution to this problem is to modify the test section to accept a longer test specimen to further remove end effects from the linear decay region. A more practical possibility, at least for the present experimental apparatus, is to generate a new, extensive data base of multiple repeat test runs from which the experimenter can, by experience, learn to discard the outlying data points at the extremities of the attenuation and phase profiles. A final possibility for propagation constant extraction is to include higher order modes excited near the specimen trailing edge in the data-fitting procedure. However, to take full advantage of this possibility, the axial resolution of pressure attenuation and phase profiles would need to be increased substantially. In addition, transverse measurements would be helpful to further isolate which higher order modes to include. As remarked previously, exploratory transverse measurements did not reveal the existence of any higher order modes, at least for the "clean" test data. Thus, for this particular experimental setup, this refinement would appear nonproductive.

The results of this limited validation experiment are encouraging despite the measured propagation constant variability and dramatic sensitivity changes exhibited by the math model. The investigation has shown that grazing-incidence impedance measurements for both downstream and upstream propagation are generally consistent with normal-incidence impedance measurements for a test specimen that would not be expected to exhibit significant effect of flow or sound pressure level. Further work needs to be done to find a consistent and objective means to extract propagation constants from the test specimen axial attenuation and phase profiles. Also, a next stage in the validation of the shear-flow model which forms the analytical basis of this method should be a comparison of results using the present method with those obtained by an *in situ* method for a linear, homogeneous, locally reacting test specimen that exhibits consistent changes in impedance due to flow.

Concluding Remarks

The infinite-wave-guide method was used to conduct a limited validation test on a two-dimensional shear-flow analytical model for determining the acoustic impedance of an acoustic liner test specimen in a grazing-incidence, grazing-flow environment. This method requires, in the present application, that the test specimen be effectively infinite in length, acoustically linear, homogeneous, and locally reacting. Also, the specimen would be expected to exhibit changes in impedance due to grazing flow. In the present experiment, however, a test specimen was purposely chosen to exhibit minimal effects of grazing flow so that the analytical model could be exercised and the resulting "measured" grazing-incidence impedance compared with carefully documented normal-incidence impedance measurements.

The analytical model was exercised at three levels of complexity which included uniform, one-dimensional shear, and two-dimensional shear-flow profiles. Inferred impedances for both downstream and upstream sound propagation were generally in good agreement with the normal-incidence impedances, regardless of the level of flow profile description complexity used in the analytical model. For upstream propagation, the impedance exhibited slightly more scatter than for the downstream propagation tests, even though the measured upstream propagation constants were of higher quality. Overall, the consistency of the results suggests that the analytical model can be confidently relied upon to infer changes in the impedance of acoustic materials subjected to grazing-incidence sound and flow. For this test specimen, the two-dimensional shear-flow model provides modestly improved agreement with normal-incidence results over that of the one-dimensional model.

Perhaps the most disconcerting aspect of these tests was the wide ranging sensitivity of the grazing-incidence impedance to relatively small changes in the measured propagation constant for certain regions of the impedance plane. In this experiment, the lowest propagation constant variability consistently attained was about 5 percent for either the

attenuation or the phase component. A great portion of this variability was thought to be due to the procedure used to extract the slopes of the "linear" regions of the attenuation and phase profiles. Therefore, further validation work should concentrate upon improving the consistency of the propagation constant extraction technique. However, error analysis suggests that the analytical model is reliable if due consideration is given to sensitivity to variability in measured propagation constant.

NASA Langley Research Center
Hampton, VA 23665-5225
March 2, 1987

References

1. Sivian, L. J.: Sound Propagation in Ducts Lined With Sound Absorbing Material. *J. Acoust. Soc. America*, vol. 9, no. 2, Oct. 1937, pp. 135–140.
2. Proceedings of the Aircraft Noise Symposium—Acoustical Duct Treatments for Aircraft. *J. Acoust. Soc. America*, vol. 48, no. 3 (Part 3), Sept. 1970.
3. Nayfeh, Ali H.; Kaiser, John E.; and Telionis, Demetri P.: Acoustics of Aircraft Engine-Duct Systems. *AIAA J.*, vol. 13, no. 2, Feb. 1975, pp. 130–153.
4. Vaidya, P. G.; and Dean, P. D.: State of the Art of Duct Acoustics. AIAA-77-1279, Oct. 1977.
5. Lowson, M. V.: Duct Acoustics and Mufflers. *Aircraft Noise Generation, Emission and Reduction*, AGARD-LS-77, June 1975, pp. 7-1–7-34.
6. Melling, T. H.: The Acoustic Impedance of Perforates at Medium and High Sound Pressure Levels. *J. Sound & Vib.*, vol. 29, no. 1, July 8, 1973, pp. 1–65.
7. Guess, A. W.: Calculation of Perforated Plate Liner Parameters From Specified Acoustic Resistance and Reactance. *J. Sound & Vib.*, vol. 40, no. 1, May 8, 1975, pp. 119–137.
8. Baumeister, Kenneth J.; and Rice, Edward J.: *Visual Study of the Effect of Grazing Flow on the Oscillatory Flow in a Resonator Orifice.* NASA TM X-3288, 1975.
9. Rice, Edward J.: *A Theoretical Study of the Acoustic Impedance of Orifices in the Presence of a Steady Grazing Flow.* NASA TM X-71903, [1976].
10. Panton, Ronald L.; and Goldman, Allen L.: Correlation of Nonlinear Orifice Impedance. *J. Acoust. Soc. America*, vol. 60, no. 6, Dec. 1976, pp. 1390–1396.
11. Kompenhans, Jurgen: Das Akustische Verhalten Uberströmter Öffnungen in Abhängigkeit von der Wandgrenzschicht, eine Experimentelle Untersuchung. Doctoral Dissertation, Goettingen University, Goettingen, West Germany, 1976. (Translation available as NASA TM-75146, 1977.)
12. Hersh, A. S.; and Walker, B.: Effect of Grazing Flow on the Acoustic Impedance of Interacting Cavity-Backed Orifices. AIAA-77-1336, Oct. 1977.
13. Lester, Harold C.; and Posey, Joe W.: *Optical One-Section and Two-Section Circular Sound-Absorbing Duct Liners for Plane-Wave and Monopole Sources Without Flow.* NASA TN D-8348, 1976.
14. Feder, Ernest; and Dean, Lee Wallace, III: *Analytical and Experimental Studies for Predicting Noise Attenuation in Acoustically Treated Ducts for Turbofan Engines.* NASA CR-1373, 1969.
15. Dean, P. D.: An In Situ Method of Wall Acoustic Impedance Measurement in Flow Ducts. *J. Sound & Vib.*, vol. 34, no. 1, May 8, 1974, pp. 97–130.
16. Zandbergen, T.: On the Practical Use of Three-Microphone Technique for In-Situ Acoustic Impedance Measurements on Double Layer Flow Duct Liners. AIAA-81-2000, Oct. 1981.
17. Syed, A. A.; Motsinger, R. E.; Fiske, G. H.; Joshi, M. C.; and Kraft, R. E.: *Turbofan Aft Duct Suppressor Study.* NASA CR-175067, 1983.
18. Armstrong, D. L.; Beckemeyer, R. J.; and Olsen, R. F.: Impedance Measurements of Acoustic Duct Liners With Grazing Flow. Boeing paper presented at the 87th Meeting of the Acoustical Society of America (New York, NY), Apr. 1974.
19. Watson, Willie R.: *A Method for Determining Acoustic-Linear Admittance in Ducts With Sheared Flow in Two Cross-Sectional Directions.* NASA TP-2518, 1985.
20. Unruh, J. F.; and Eversman, W.: The Transmission of Sound in an Acoustically Treated Rectangular Duct With Boundary Layer. *J. Sound & Vib.*, vol. 25, no. 3, Dec. 1972, pp. 371–382.
21. Zwikker, C.; and Kosten, C. W.: *Sound Absorbing Materials.* Elsevier Publ. Co., Inc., 1949.
22. Tijdeman, H.: On the Propagation of Sound Waves in Cylindrical Tubes. *J. Sound & Vib.*, vol. 39, no. 1, Mar. 1975, pp. 1–33.
23. Parrott, Tony L.; and Smith, C. D.: *Random and Systematic Measurement Errors in Acoustic Impedance as Determined by the Transmission Line Method.* NASA TN D-8520, 1977.
24. Hubbard, Harvey H.; and Manning, James C.: *Aeroacoustic Research Facilities at NASA Langley Research Center—Description and Operational Characteristics.* NASA TM-84585, 1983.
25. Parrott, Tony L.; and Jones, Michael G.: *Pressure Probe and Hot-Film Responses to Acoustic Excitation in Mean Flow.* NASA TP-2581, 1986.
26. Parrott, Tony L.; and Lester, Harold C.: Calculated and Measured Performance of a "Near Ideal" Locally Reacting Duct Liner in Grazing Incidence. AIAA-80-0989, June 1980.

Table I. Variability of Normal-Incidence Impedance of Test Specimen

Frequency, kHz	Position 1		Position 2		Position 3		Position 4		Average		Maximum absolute variability		Maximum relative variability	
	θ_1	χ_1	θ_2	χ_2	θ_3	χ_3	θ_4	χ_4	θ_{avg}	χ_{avg}	$\Delta\theta$	$\Delta\chi$	$\Delta\theta/\theta_{avg}$	$\Delta\chi/\chi_{avg}$
0.5	0.4013	−1.2780	0.4367	−1.2946	0.4203	−1.3459	0.4088	−1.3046	0.4168	−1.3058	0.0199	0.0401	0.0478	0.0307
.6	.3872	−.9089	.4078	−.9229	.3909	−.9188	.3724	−.8911	.3896	−.9104	.0182	.0193	.0468	.0212
.7	.3808	−.5796	.4007	−.6031	.4051	−.6170	.3676	−.5630	.3886	−.5907	.0210	.0277	.0539	.0469
.8	.3973	−.2982	.4125	−.3267	.4145	−.3008	.3829	−.2824	.4018	−.3020	.0189	.0247	.0470	.0817
.9	.4293	−.0319	.4370	−.0542	.4519	−.0816	.4143	.0095	.4331	−.0396	.0188	.0491	.0435	1.2402
1.0	.4682	.1431	.4960	.2423	.4962	.2410	.4586	.2190	.4798	.2113	.0211	.0683	.0441	.3229
1.1	.5489	.4434	.5753	.4686	.5915	.5211	.5363	.4659	.5630	.4748	.0285	.0463	.0506	.0976
1.2	.6506	.6989	.6800	.7154	.6955	.7807	.5783	.6423	.6511	.7093	.0728	.0714	.1118	.1006
1.3	.8349	.9854	.8289	.9679	.8667	1.0643	.7801	.9854	.8277	1.0008	.0476	.0635	.0575	.0635
1.4	1.0013	1.2280	1.0143	1.2295	1.1042	1.3630	1.0366	1.2960	1.0391	1.2791	.0651	.0839	.0627	.0656
1.5	1.5575	1.5919	1.3872	1.5339	1.4109	1.6527	1.3735	1.5958	1.4323	1.5936	.1252	.0597	.0874	.0374
1.6	1.8487	1.7925	1.9085	1.8041	2.0321	1.9383	1.7285	1.8242	1.8794	1.8398	.1526	.0985	.0812	.0536
1.7	3.1674	1.6361	2.9005	1.8001	3.1266	1.9027	2.8235	1.9094	3.0045	1.8121	.1810	.1760	.0602	.0971
1.8	3.5882	1.4484	3.8223	1.2250	3.8618	1.5354	3.8861	1.3184	3.7896	1.3818	.2014	.1568	.0531	.1135
1.9	4.2638	−.1140	4.3367	.3053	4.5523	.2678	4.4164	.2481	4.3923	.1768	.1600	.2908	.0364	1.6448
2.0	3.6399	−1.3137	3.9078	−1.1242	3.8619	−1.4609	3.8442	−1.3000	3.8135	−1.2997	.1736	.1755	.0455	.1350
2.1	2.6997	−1.7422	2.8197	−1.7935	2.9609	−1.8362	2.7006	−1.8346	2.7952	−1.8016	.1657	.0594	.0593	.0330
2.2	2.0210	−1.6897	2.0956	−1.7467	1.9802	−1.8022	2.0049	−1.7614	2.0254	−1.7500	.0702	.0603	.0346	.0345
2.3	1.3963	−1.4224	1.4482	−1.4764	1.4151	−1.5012	1.3273	−1.4533	1.3967	−1.4633	.0694	.0409	.0497	.0280
2.4	1.0968	−1.1638	1.2334	−1.2394	1.1946	−1.2337	1.0676	−1.1718	1.1481	−1.2022	.0853	.0384	.0743	.0319
2.5	.9704	−.9260	.9027	−.9027	0.9773	−.9440	.8792	−.8952	.9324	−.9170	.0532	.0270	.0571	.0295
2.6	.7842	−.6530	.8089	−.6705	.8432	−.6796	.7509	−.6225	.7968	−.6564	.0464	.0339	.0582	.0516
2.7	.7029	−.4009	.7189	−.4129	.7517	−.4187	.7035	−.4045	.7193	−.4093	.0324	.0094	.0451	.0231
2.8	.6742	−.1820	.6983	−.2125	.7119	−.1722	.6712	−.1879	.6889	−.1887	.0230	.0238	.0334	.1264
2.9	.6779	.0139	.6986	−.0129	.7201	.0161	.6692	.0049	.6914	.0055	.0286	.0184	.0414	3.3455
3.0	.6911	.1690	.7365	.2109	.7704	.2848	.6968	.2307	.7237	.2239	.0467	.0609	.0645	.2723

Table II. Impedances Obtained From Computational Models and From Normal-Incidence Measurements

(a) Downstream sound propagation (driver located upstream of LE)

Frequency, kHz	Uniform		1-D shear		2-D shear		Normal incid.	
	θ	χ	θ	χ	θ	χ	θ	χ
$M_{C/L} = 0$								
0.5	0.399	−1.268	0.399	−1.268	0.399	−1.268	0.412	−1.306
1.0	.489	.204	.489	.204	.489	.204	.480	.211
1.5	1.549	1.620	1.549	1.620	1.549	1.620	1.432	1.594
2.0	3.438	−1.411	3.438	−1.411	3.438	−1.411	3.813	−1.300
2.5	.821	−.926	.821	−.926	.821	−.926	.932	−.917
3.0	.817	.305	.817	.305	.817	.305	.724	.224
$M_{C/L} = 0.1$								
0.5	0.437	−1.287	0.435	−1.299	0.401	−1.300	0.412	−1.306
1.0	.569	.227	.564	.214	.507	.215	.480	.211
1.5	1.015	1.526	1.034	1.533	1.110	1.610	1.432	1.594
2.0	3.721	1.520	3.851	−1.530	3.830	1.490	3.813	−1.300
2.5	.955	−.784	.991	−.842	.957	−.863	.932	−.917
3.0	.378	−.109	.397	−.098	.420	−.006	.724	.224
$M_{C/L} = 0.3$								
0.5	0.419	−1.122	0.415	−1.120	0.407	−1.180	0.412	−1.306
1.0	.474	.241	.468	.232	.471	.241	.480	.211
1.5	1.593	1.713	1.628	1.714	1.611	1.651	1.432	1.594
2.0	3.233	−1.172	3.246	−1.265	3.411	−1.255	3.813	−1.300
2.5	.845	−.769	.857	−.829	.872	−.841	.932	−.917
3.0	.662	.238	.690	.242	.710	.281	.724	.224
$M_{C/L} = 0.5$								
0.5	0.335	−0.672	0.324	−0.657	0.357	−0.644	0.412	−1.306
1.0	2.794	−3.370	2.557	−3.334	2.471	−3.271	.480	.211
1.5	1.351	1.420	1.447	1.406	1.410	1.487	1.432	1.594
2.0	3.450	−.458	3.558	−.806	3.621	−.920	3.813	−1.300
2.5	.800	−.785	.843	−.936	.871	−.922	.932	−.917
3.0	.838	.216	.753	.234	.741	.225	.724	.224

Table II. Concluded

(b) Upstream sound propagation (driver located downstream of TE)

Frequency, kHz	Uniform		1-D shear		2-D shear		Normal incid.	
	θ	χ	θ	χ	θ	χ	θ	χ
$M_{C/L} = 0$								
0.5	0.547	−1.554	0.547	−1.554	0.547	−1.554	0.412	−1.306
1.0	.489	.208	.489	.208	.489	.208	.480	.211
1.5	1.242	1.452	1.242	1.452	1.242	1.452	1.432	1.594
2.0	3.630	-1.450	3.630	−1.450	3.630	−1.450	3.813	−1.300
2.5	.815	−.928	.815	−.928	.815	−.928	.932	−.917
3.0	.826	.298	.826	.298	.826	.298	.724	.224
$M_{C/L} = 0.1$								
0.5	0.277	−1.063	0.278	−1.030	0.311	−1.120	0.412	−1.306
1.0	.492	.197	.501	.211	.491	.223	.480	.211
1.5	1.516	1.613	1.490	1.602	1.475	1.600	1.432	1.594
2.0	2.728	−2.093	2.613	−1.990	2.921	−2.010	3.813	−1.300
2.5	.848	−.911	.812	−.840	.853	−.863	.932	−.917
3.0	.810	.244	.748	.191	.752	.207	.724	.224
$M_{C/L} = 0.3$								
0.5	0.435	−1.603	0.437	−1.503	0.430	−1.470	0.412	−1.306
1.0	.575	.285	.579	.295	.565	.271	.480	.211
1.5	1.673	1.626	1.661	1.610	1.582	1.581	1.432	1.594
2.0	3.720	−1.910	3.467	−1.849	3.521	−1.790	3.813	−1.300
2.5	.834	−1.000	.849	−.935	.863	−.920	.932	−.917
3.0	1.068	.472	.992	.400	.957	.370	.724	.224
$M_{C/L} = 0.5$								
0.5	0.204	−1.982	0.356	−1.457	0.371	−1.410	0.412	−1.306
1.0	.601	.119	.633	.202	.627	.209	.480	.211
1.5	2.860	1.639	2.520	1.413	2.711	1.517	1.432	1.594
2.0	2.884	−3.178	1.940	−2.200	2.071	−2.100	3.813	−1.300
2.5	1.442	−.811	.897	−.845	.912	−.865	.932	−.917
3.0	1.832	1.160	.693	−.412	.712	−.307	.724	.224

Table III. Grazing-Incidence Impedance Variability at Mach Number of 0.3

Frequency, kHz	Slopes, a_2		Slope change		Impedance, ζ		Impedance change	
	Phase, deg/cm	Atten., dB/cm	Phase, percent	Atten., percent	θ	χ	$\delta\theta/\theta$, percent	$\delta\chi/\chi$, percent
[a]0.5	6.360	0.0868			0.404	−1.160		
.5	6.669	.0903	4.9	4.0	.340	−.985	−15.8	15.1
.5	6.520	.0903	2.5	4.0	.385	−1.028	−4.7	11.4
[a]2.0	17.280	.1614			3.420	−1.241		
2.0	17.212	.1597	−.4	−1.1	3.560	−1.069	4.1	13.9
2.0	17.023	.1597	−1.5	−1.1	3.746	−.476	9.5	61.6

[a]Baseline data (presented in figs. 25–27) with which data from the repeat test data are compared.

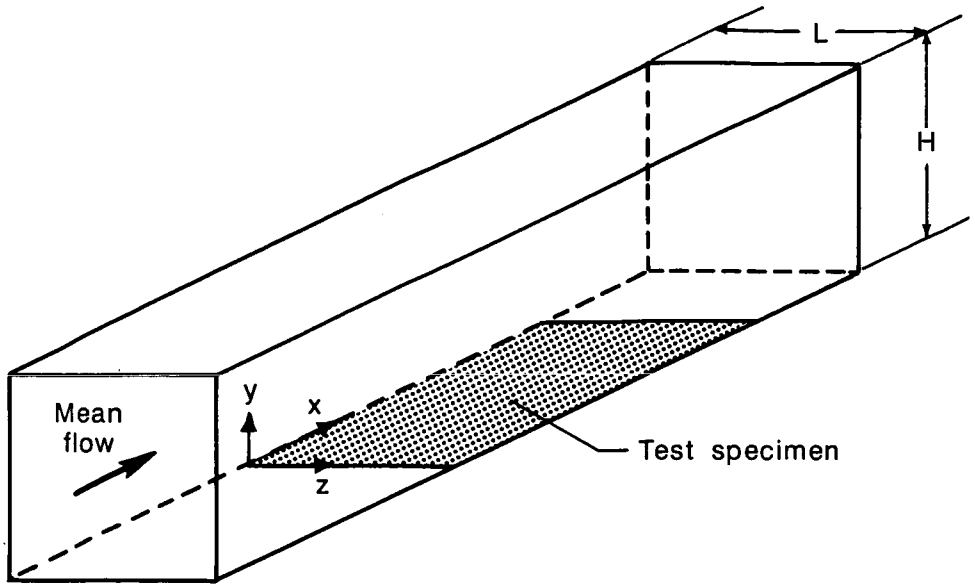

Figure 1. Schematic of geometry and coordinate system for grazing-flow impedance tube test section.

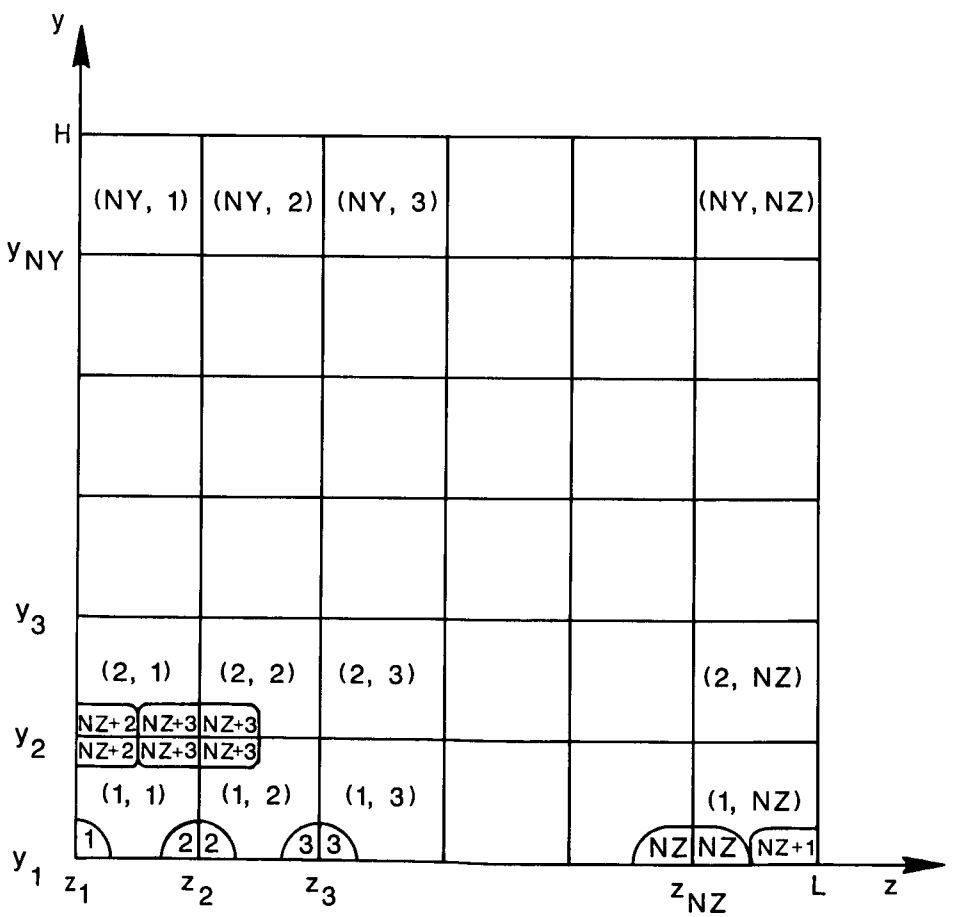

Figure 2. Diagram showing finite-element discretization scheme.

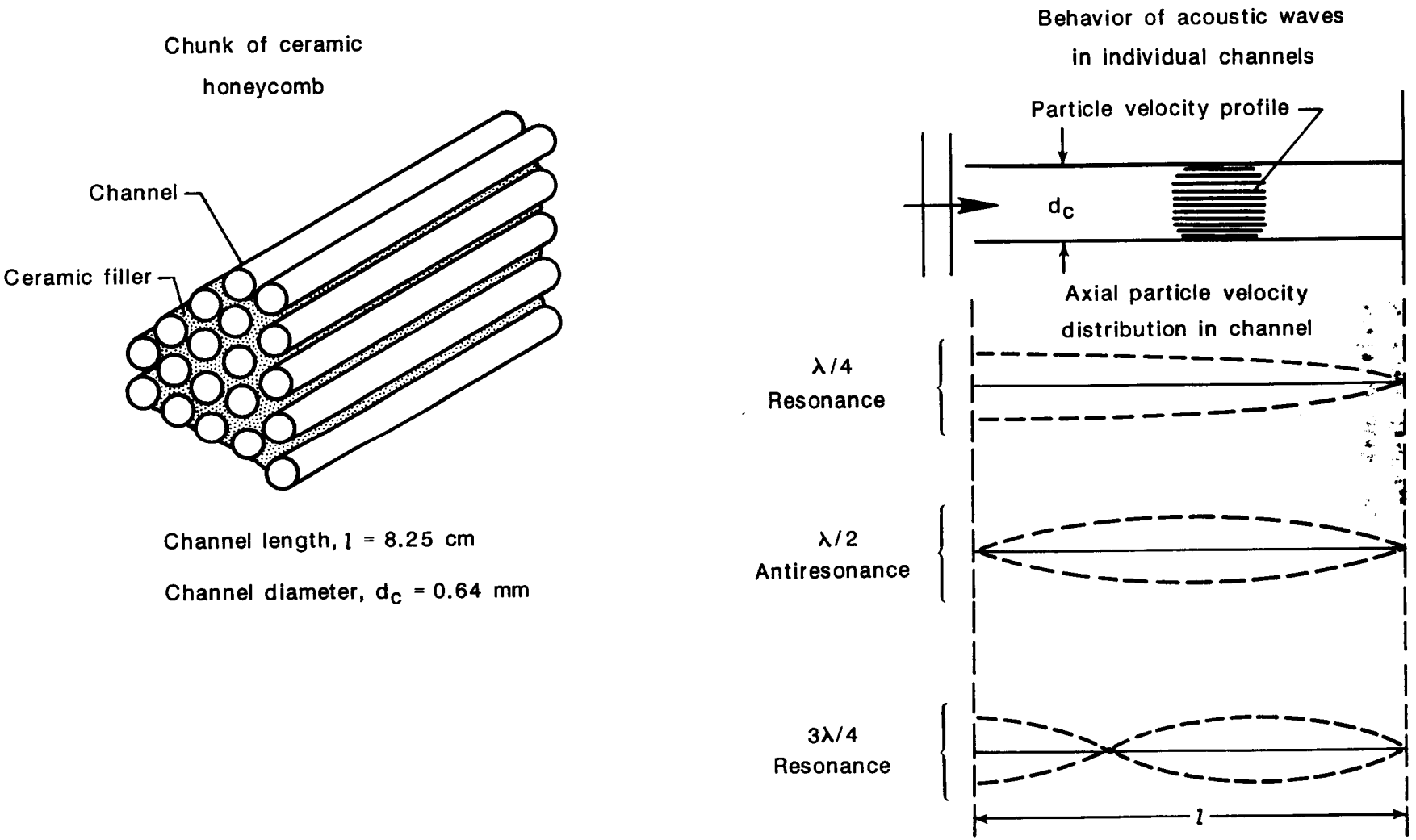

Figure 3. Schematic of ceramic honeycomb structure illustrating acoustic wave behavior in channels.

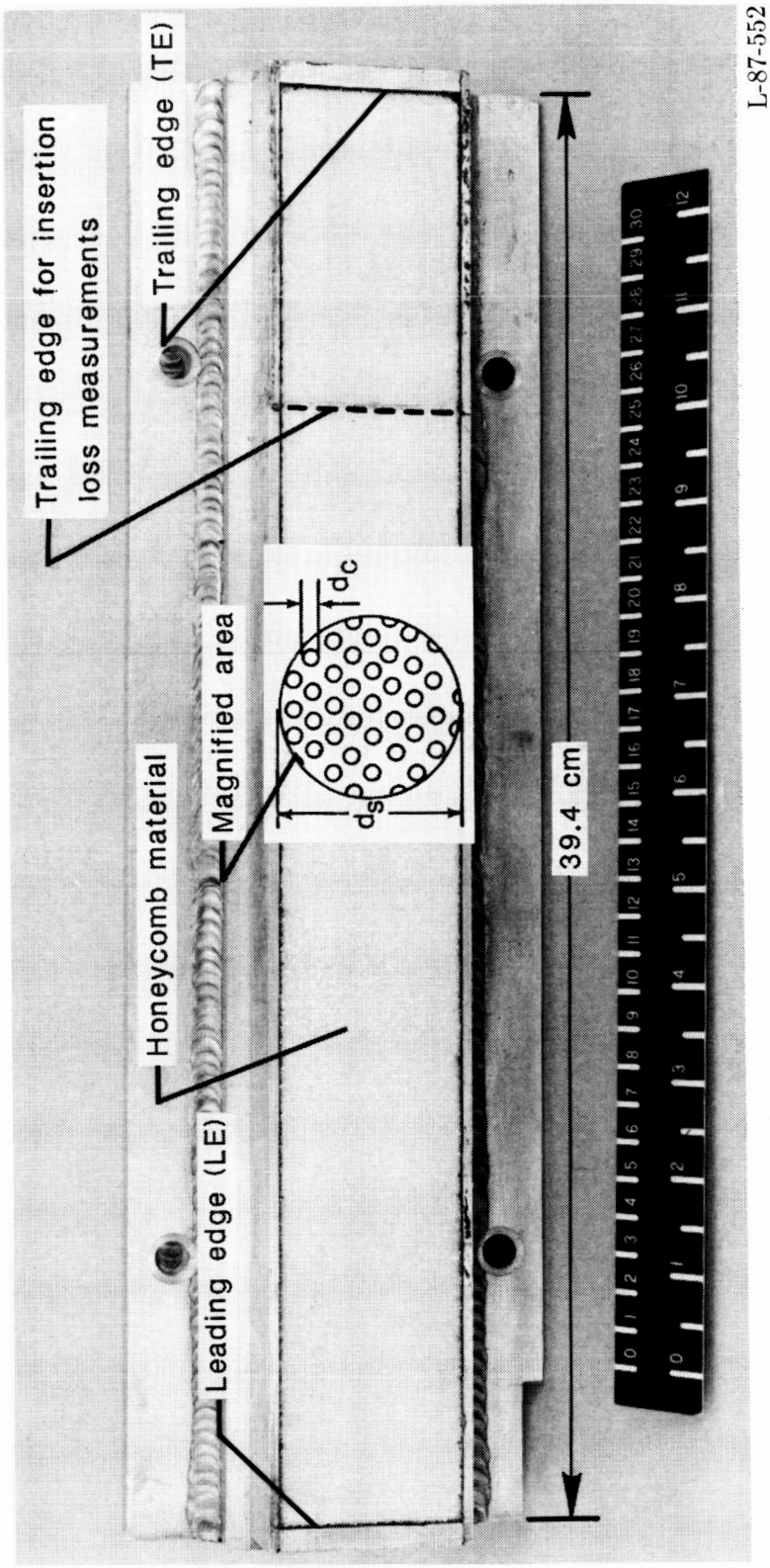

L-87-552

Figure 4. Photograph of ceramic honeycomb test specimen.

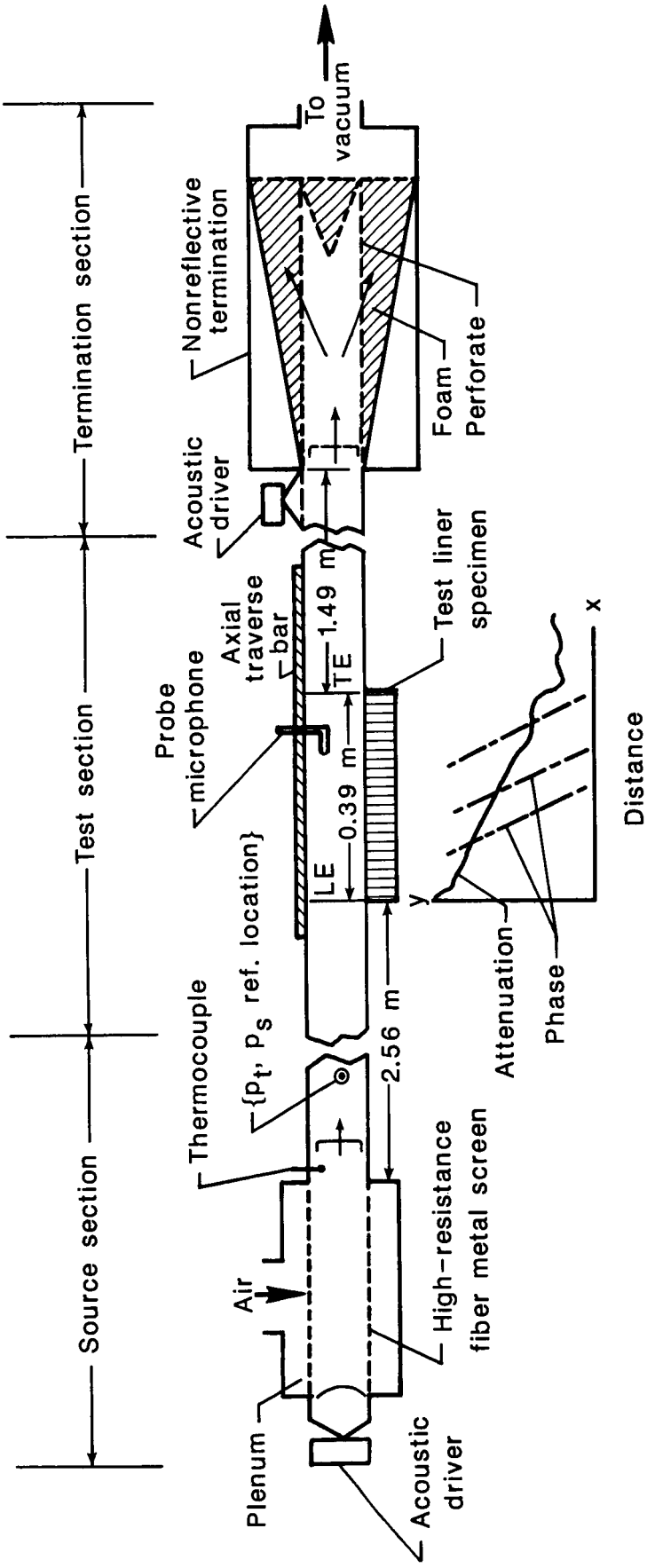

Figure 5. Schematic of experimental arrangement and instrumentation.

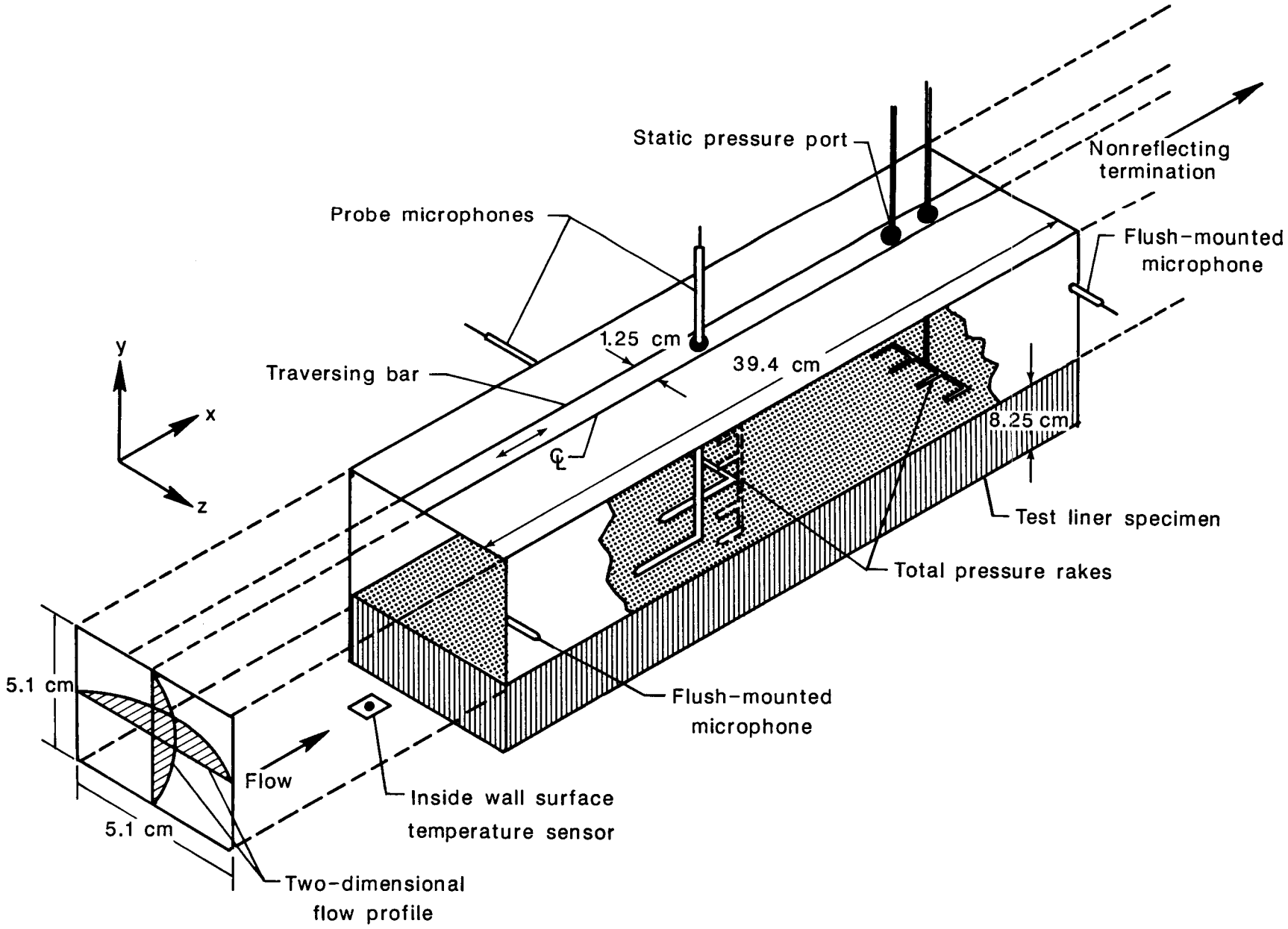

Figure 6. Details of test liner installation and instrumentation.

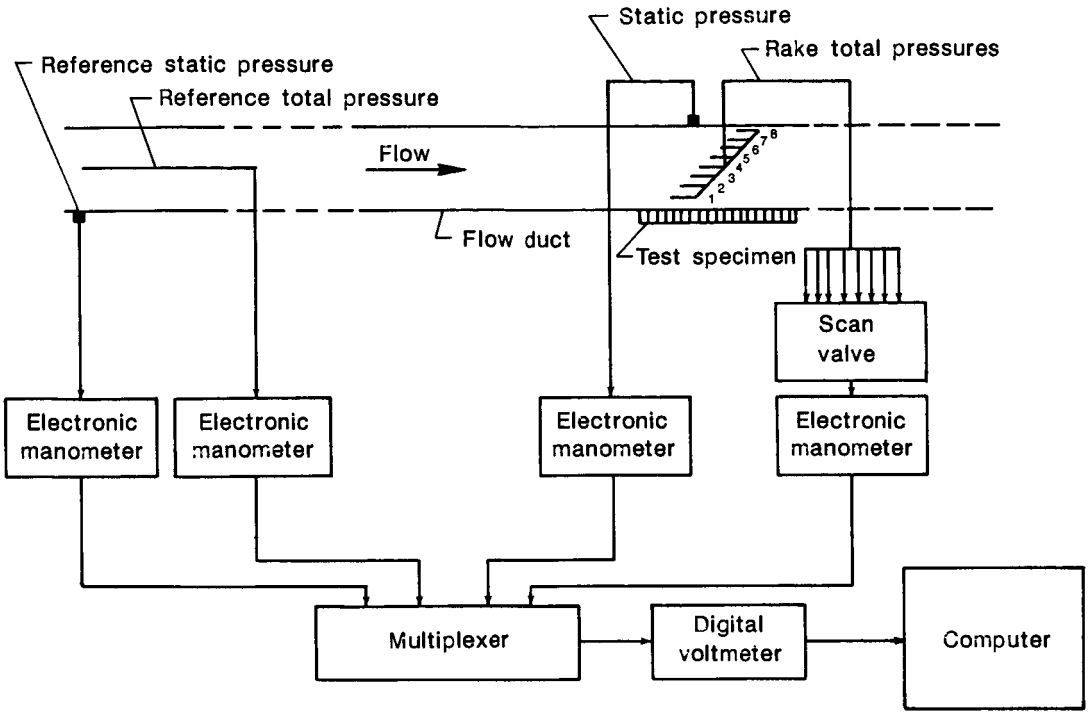

Figure 7. Diagram of flow instrumentation signal conditioning.

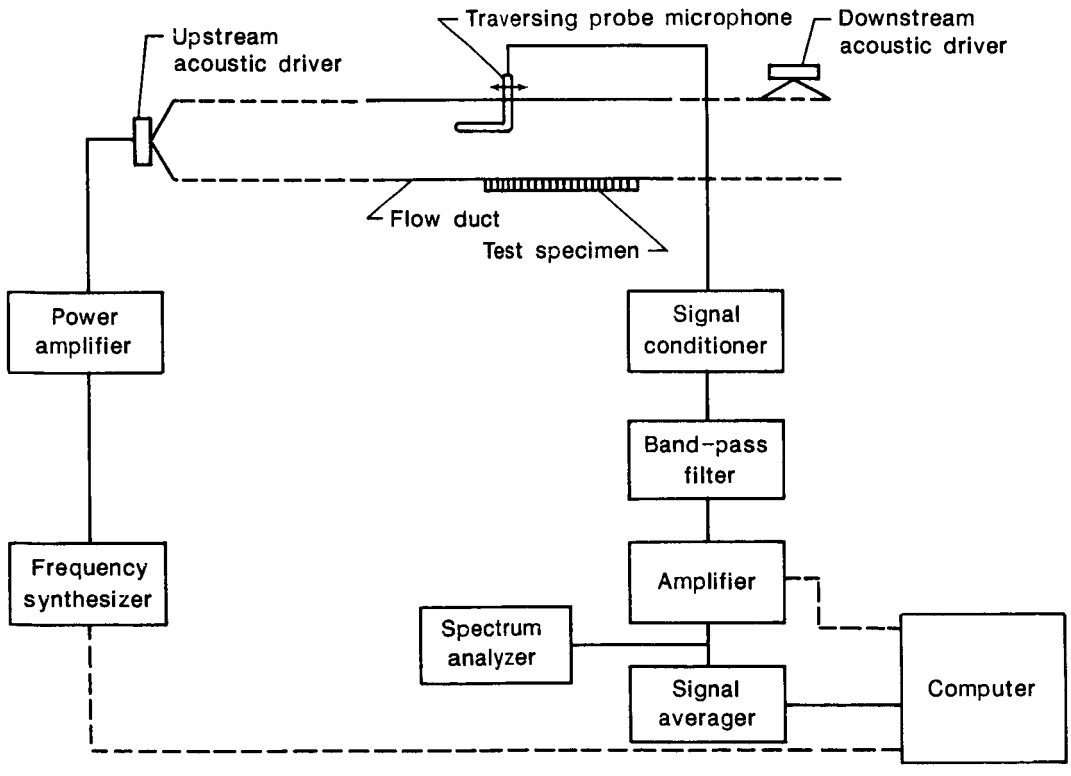

Figure 8. Diagram of acoustic signal processing.

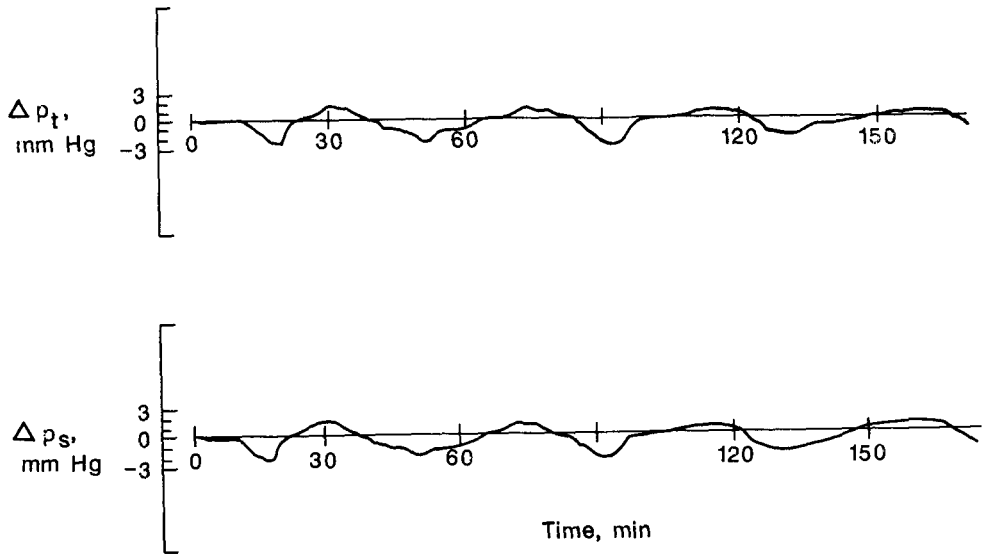

Figure 9. Variation of total and static pressure at reference location with time for nominal centerline Mach number of 0.1.

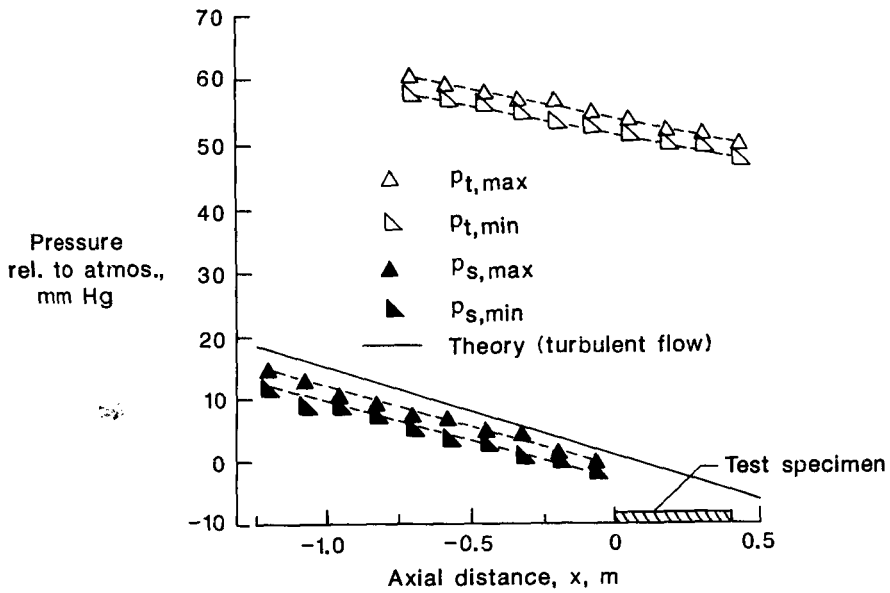

Figure 10. Axial variation of maximum and minimum total and static pressure relative to atmospheric pressure. $M_{C/L} = 0.3$ at reference location.

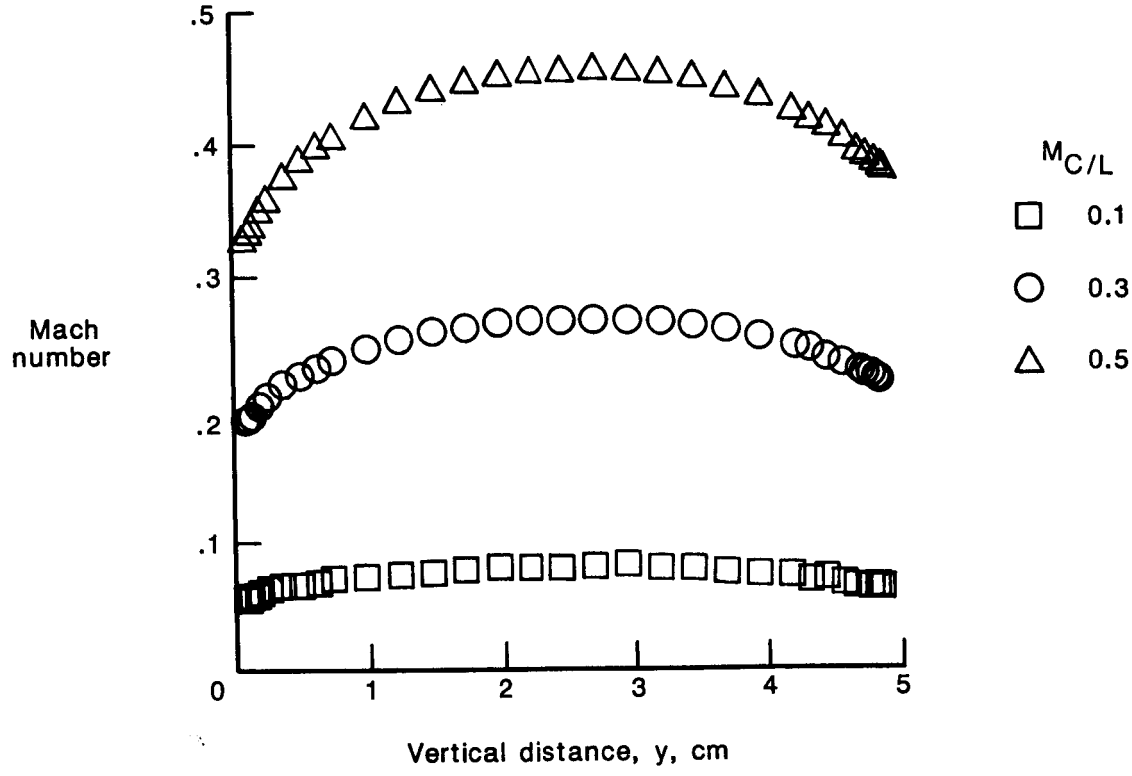

Figure 11. Comparison of vertical velocity profiles for three centerline Mach numbers at $z = 1.91$ cm and hard wall boundary conditions. $x = 20$ cm.

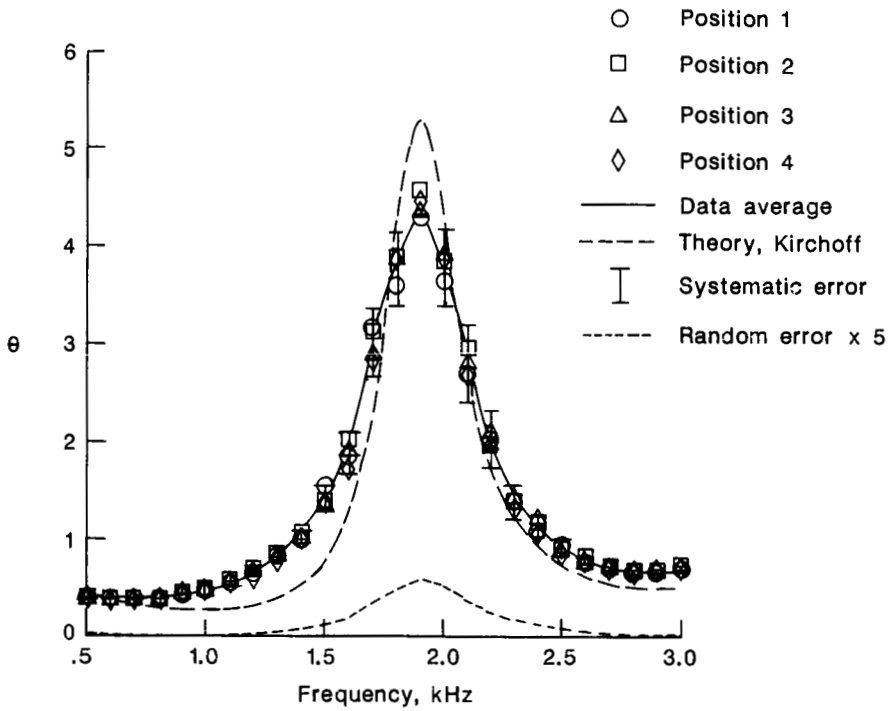

(a) Normalized acoustic resistance, θ.

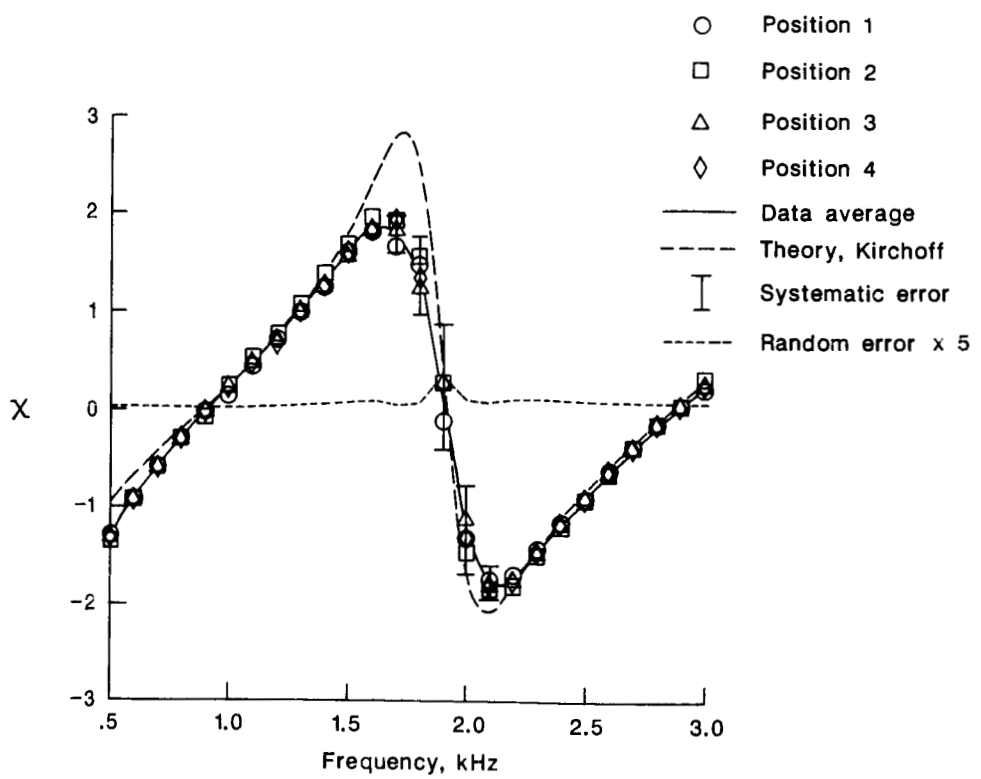

(b) Normalized acoustic reactance, χ.

Figure 12. Normal-incidence impedance of ceramic honeycomb test specimen measured at four axial locations.

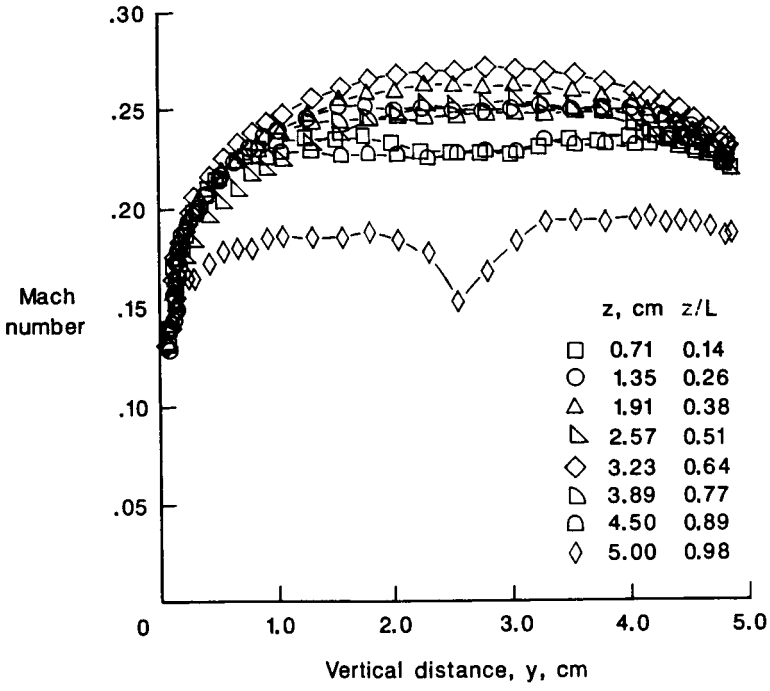

(a) At test specimen leading edge. $x = 0$; $M_{C/L} = 0.3$.

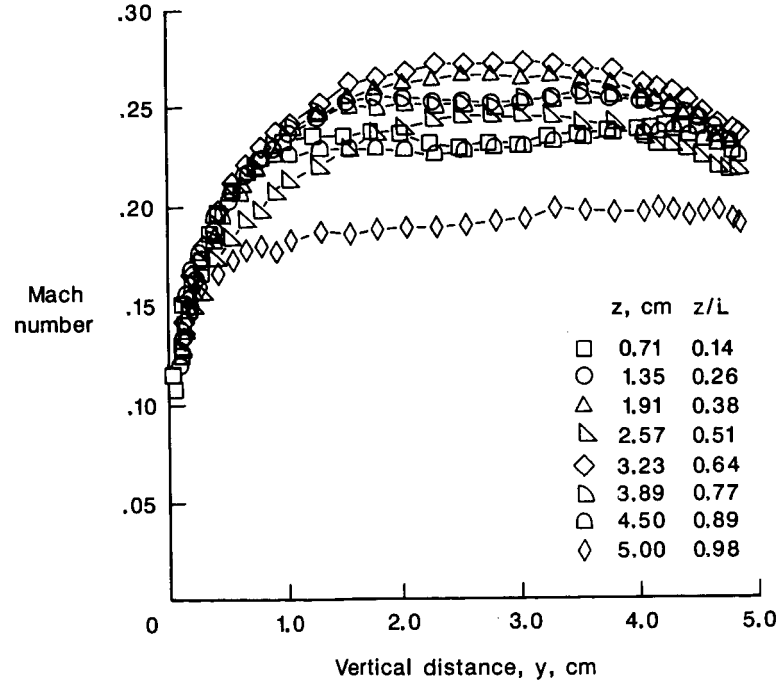

(b) At test specimen trailing edge. $x = 39.4$ cm; $M_{C/L} = 0.3$.

Figure 13. Vertical flow profiles over ceramic honeycomb test specimen.

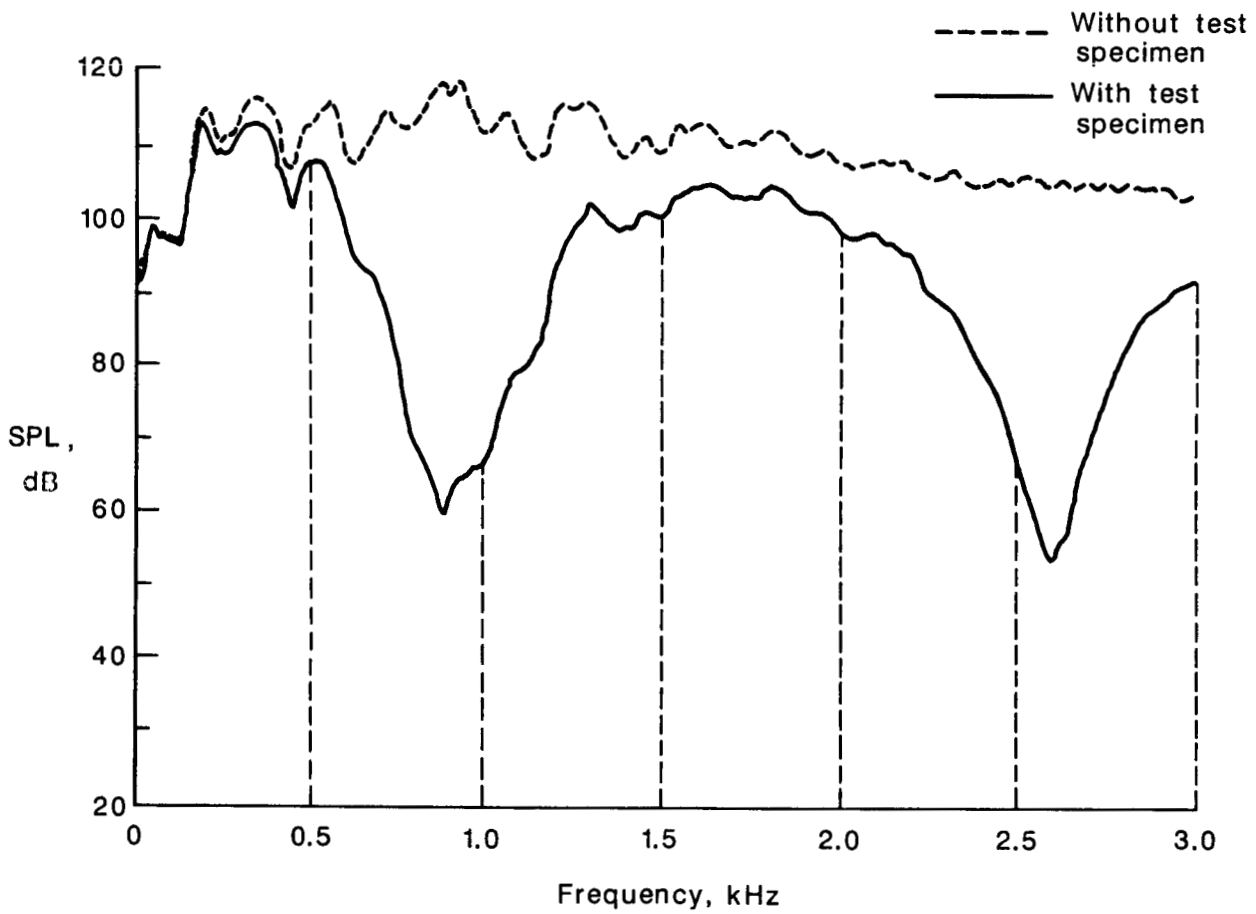

Figure 14. Attenuation spectrum for ceramic honeycomb with designated test frequencies for grazing-flow impedance measurement.

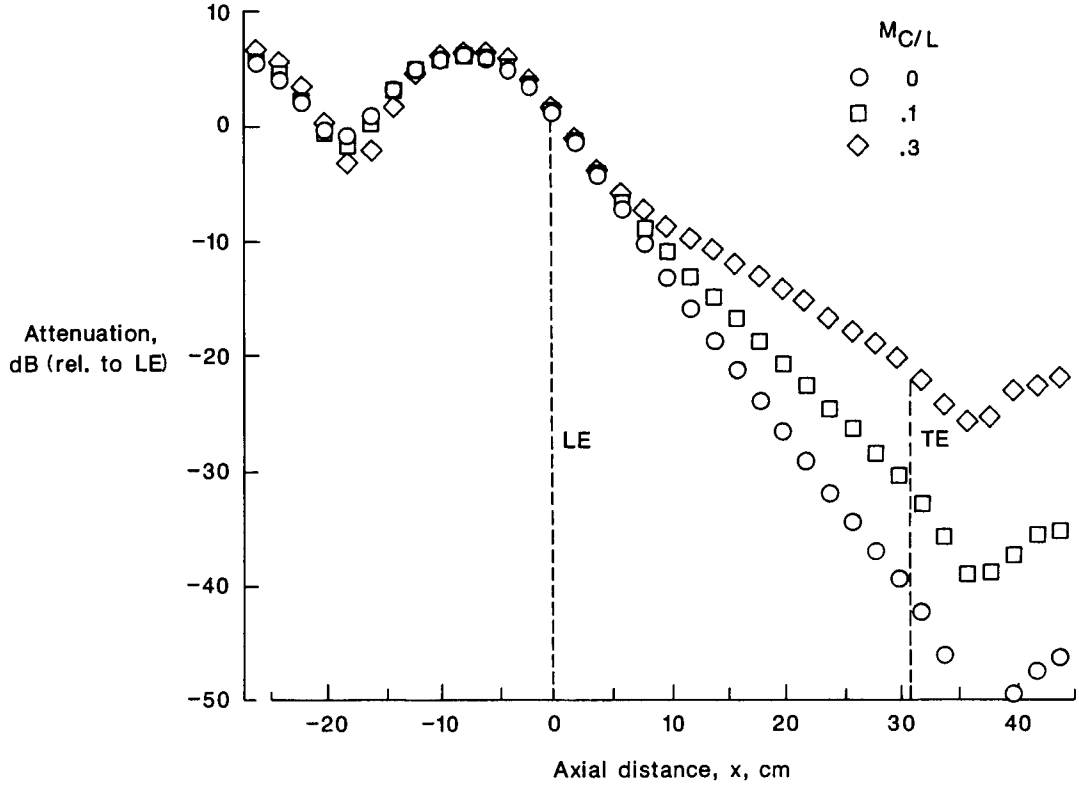

(a) Axial attenuation relative to test specimen leading edge at 0.8 kHz.

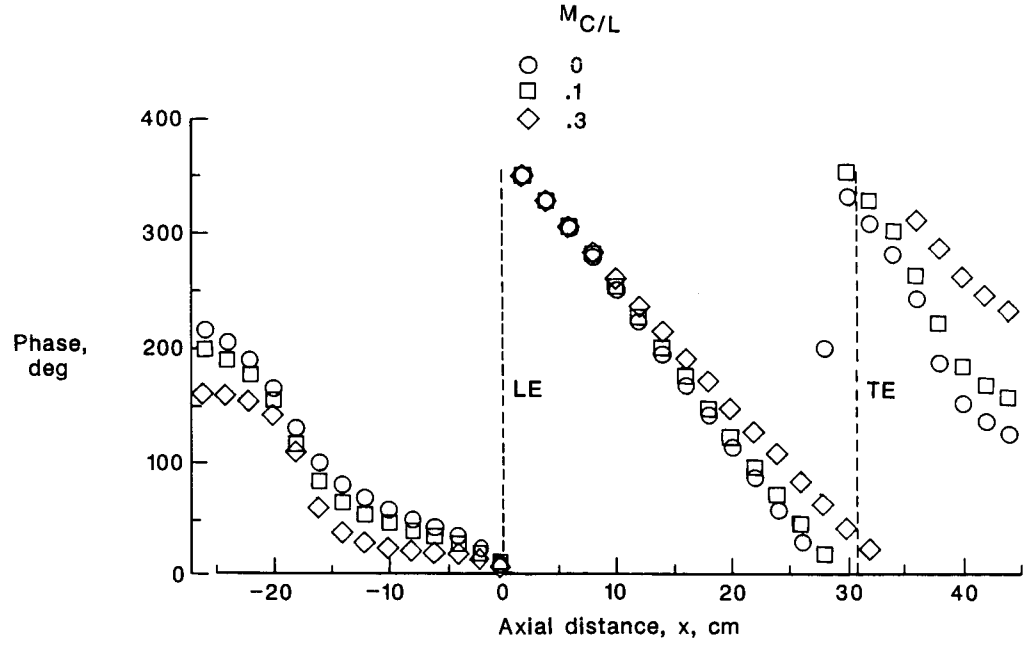

(b) Axial phase profile at 0.8 kHz.

Figure 15. Effect of flow on measured propagation constant.

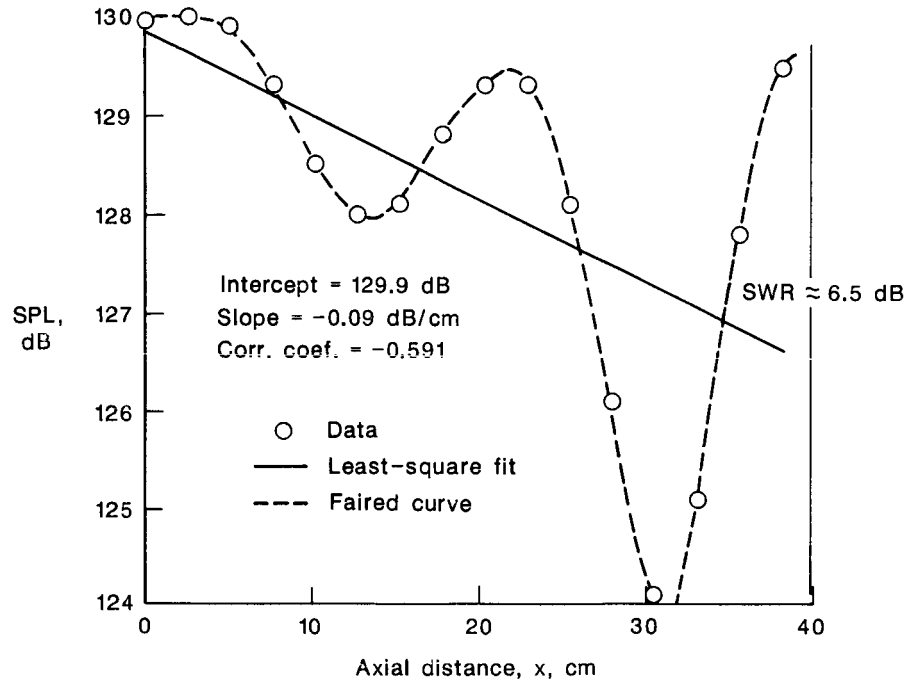

(a) Sound pressure level attenuation profile.

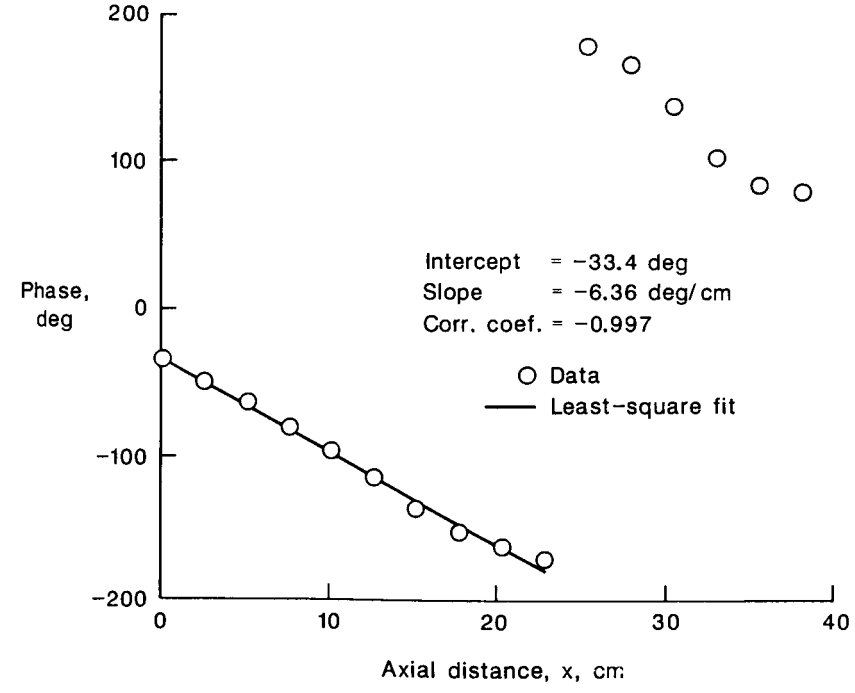

(b) Phase profile.

Figure 16. Measured axial acoustic pressure profile at Mach number of 0.3, frequency of 0.5 kHz, and downstream propagation.

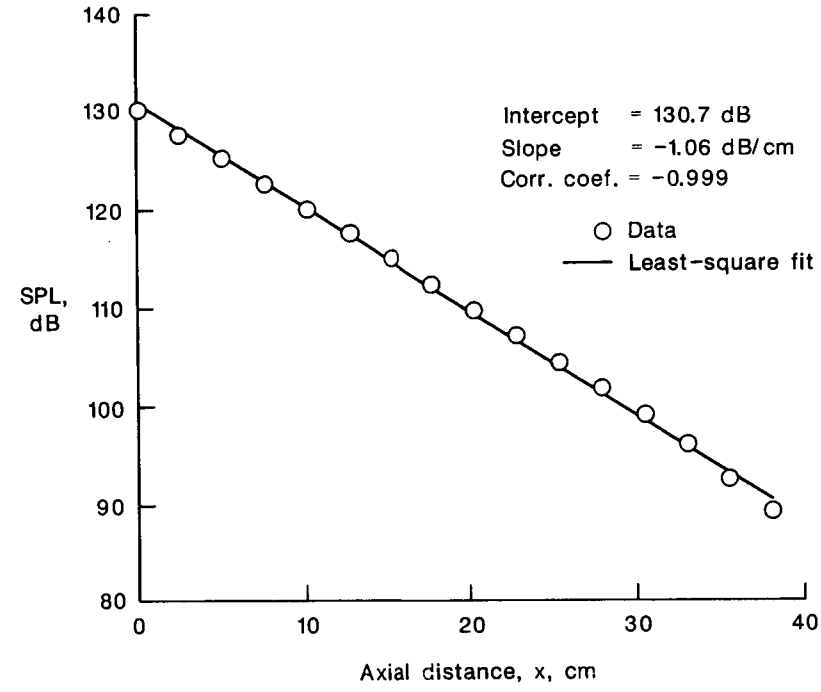

(a) Sound pressure level attenuation profile.

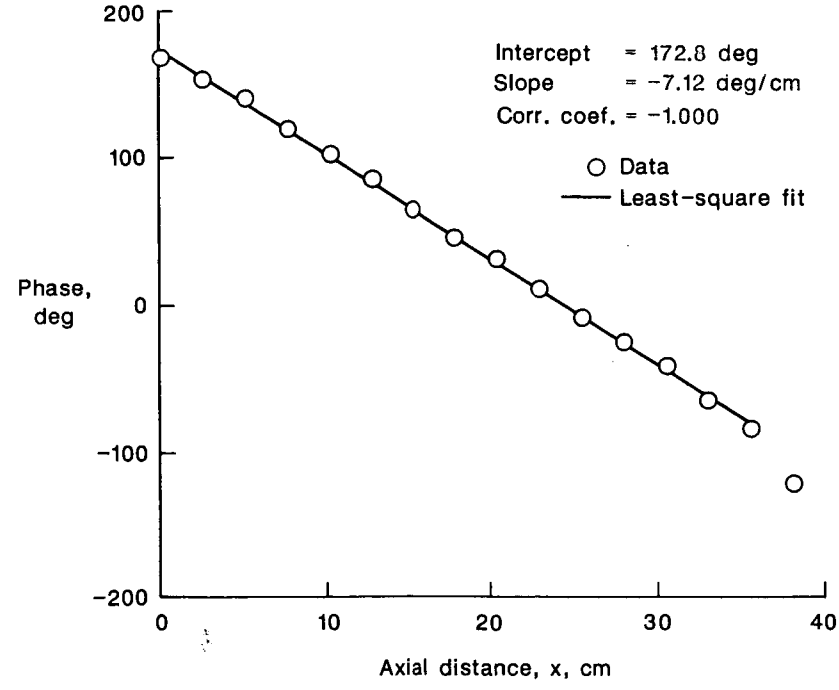

(b) Phase profile.

Figure 17. Measured axial acoustic pressure profile at Mach number of 0.3, frequency of 1.0 kHz, and downstream propagation.

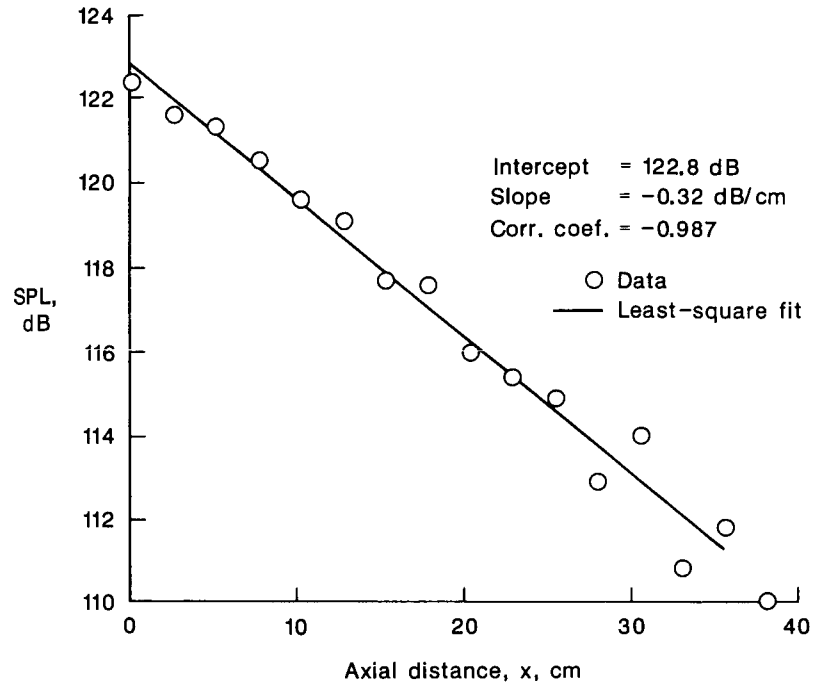

(a) Sound pressure level attenuation profile.

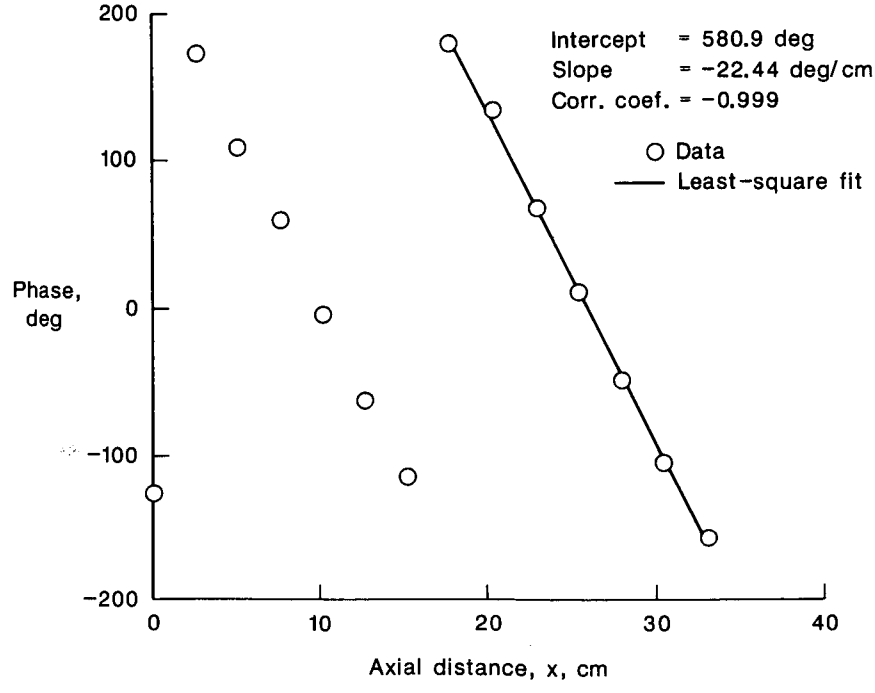

(b) Phase profile.

Figure 18. Measured axial acoustic pressure profile at Mach number of 0.3, frequency of 3.0 kHz, and downstream propagation.

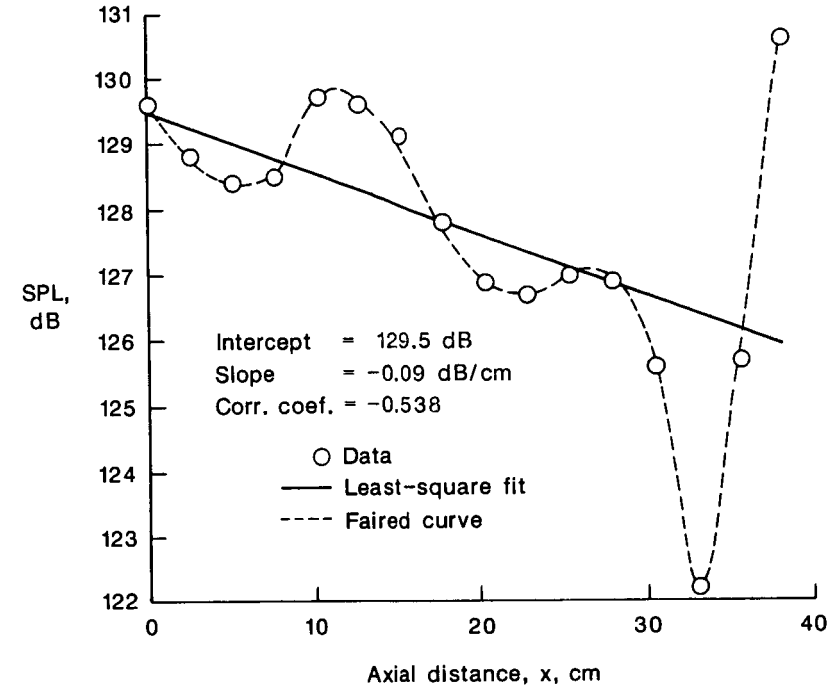

(a) Sound pressure level attenuation profile.

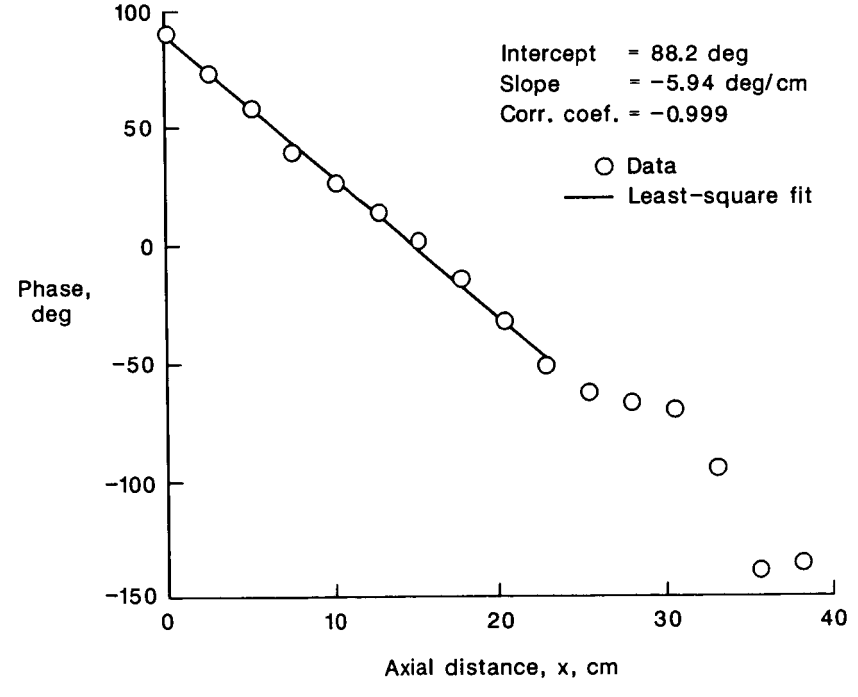

(b) Phase profile.

Figure 19. Measured axial acoustic pressure profile at Mach number of 0.5, frequency of 0.5 kHz, and downstream propagation.

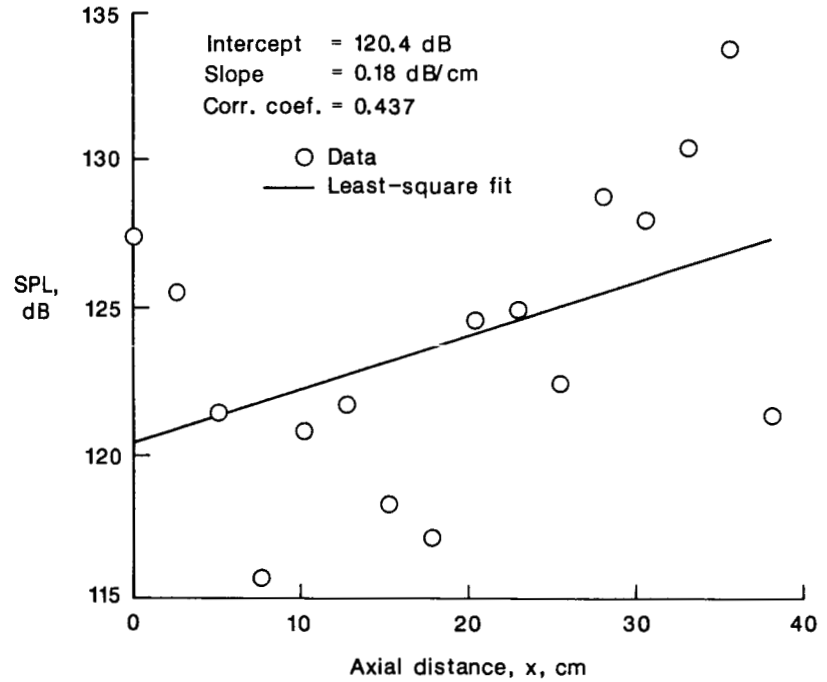

(a) Sound pressure level attenuation profile.

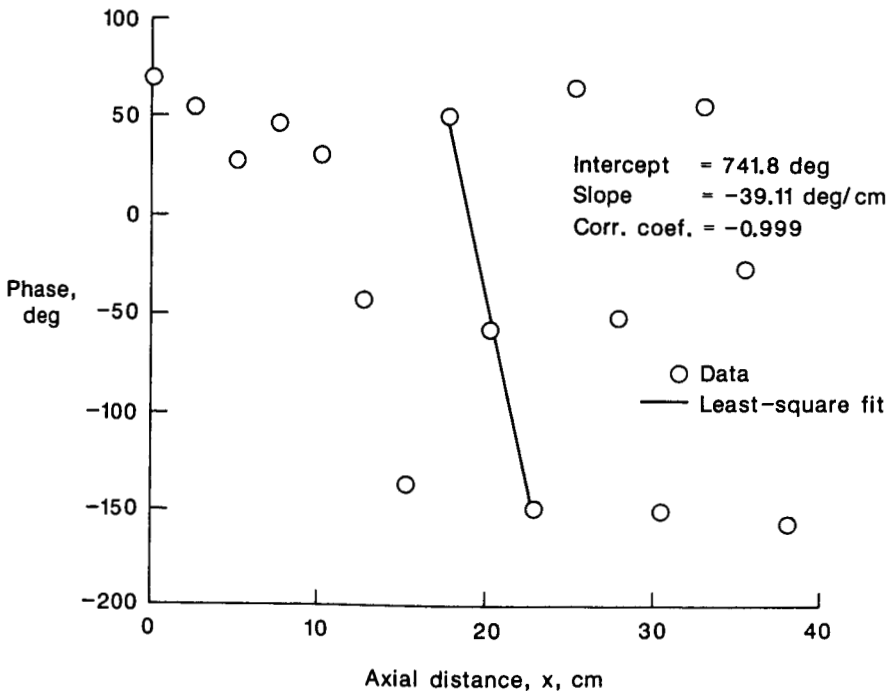

(b) Phase profile.

Figure 20. Measured axial acoustic pressure profile at Mach number of 0.5, frequency of 1.0 kHz, and downstream propagation.

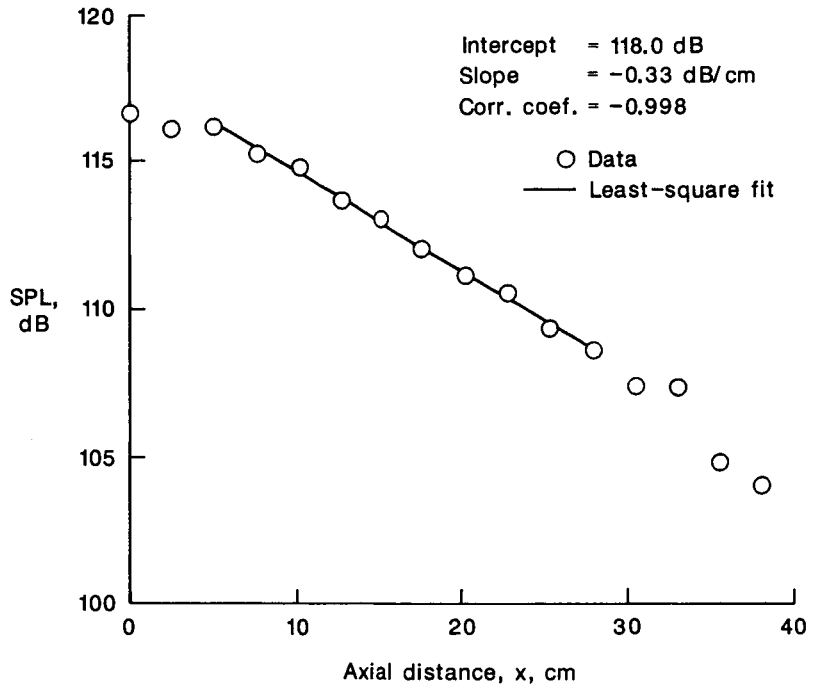

(a) Sound pressure level attenuation profile.

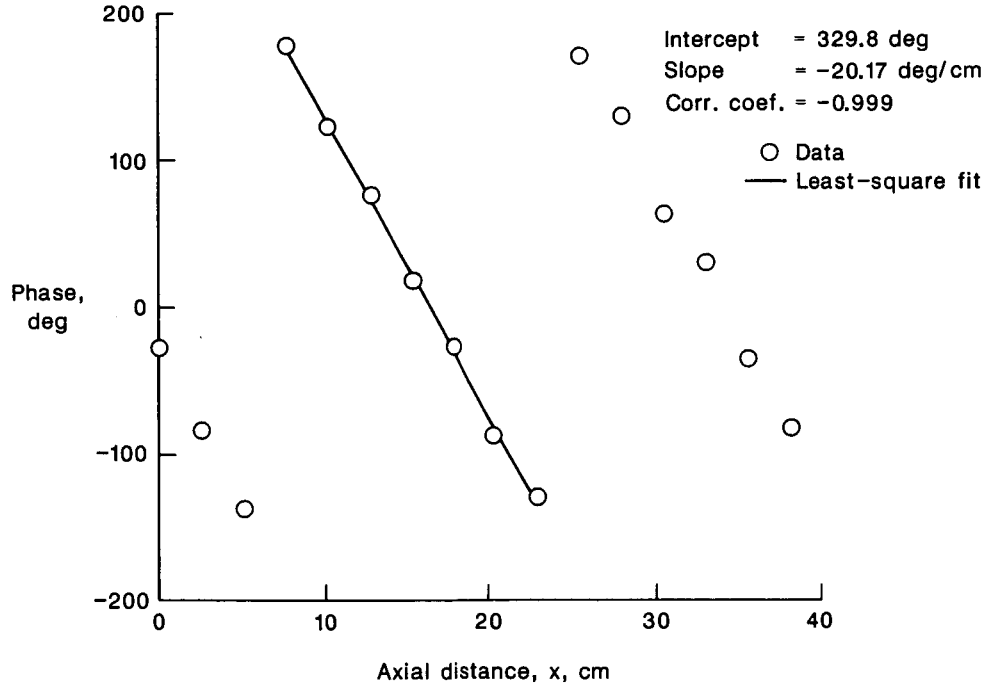

(b) Phase profile.

Figure 21. Measured axial acoustic pressure profile at Mach number of 0.5, frequency of 3.0 kHz, and downstream propagation.

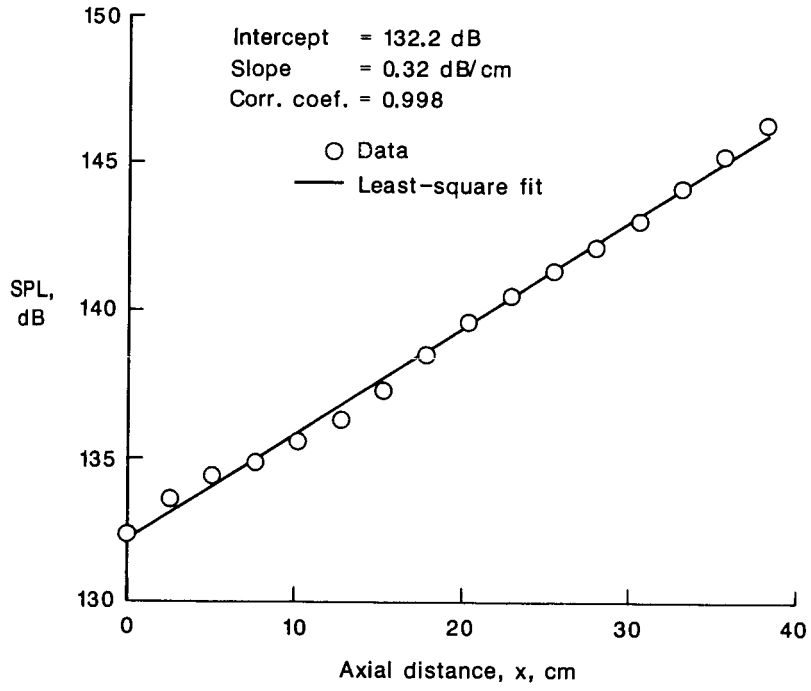

(a) Sound pressure level attenuation profile.

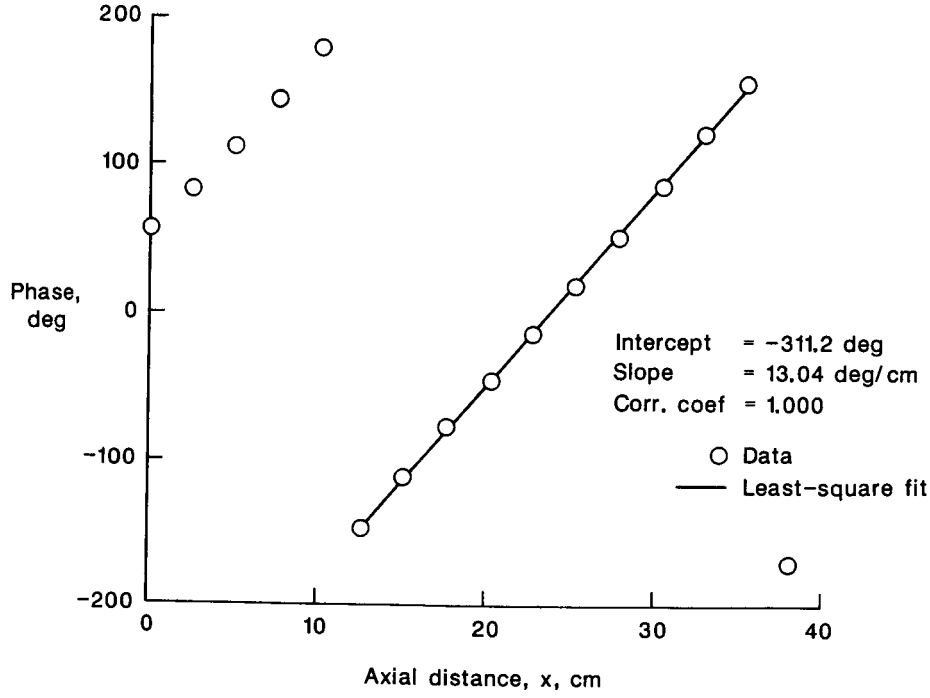

(b) Phase profile.

Figure 22. Measured axial acoustic pressure profile at Mach number of 0.3, frequency of 0.5 kHz, and upstream propagation.

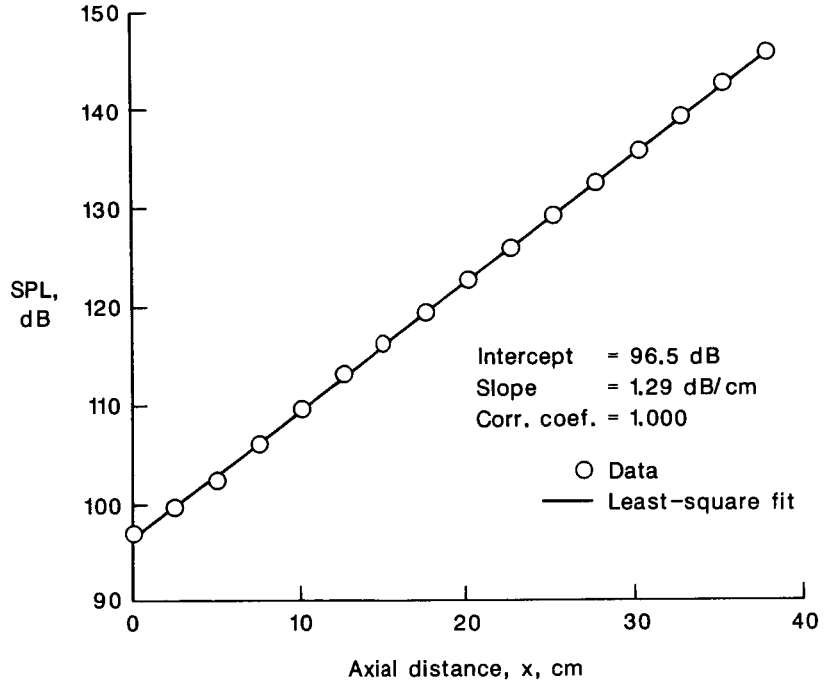

(a) Sound pressure level attenuation profile.

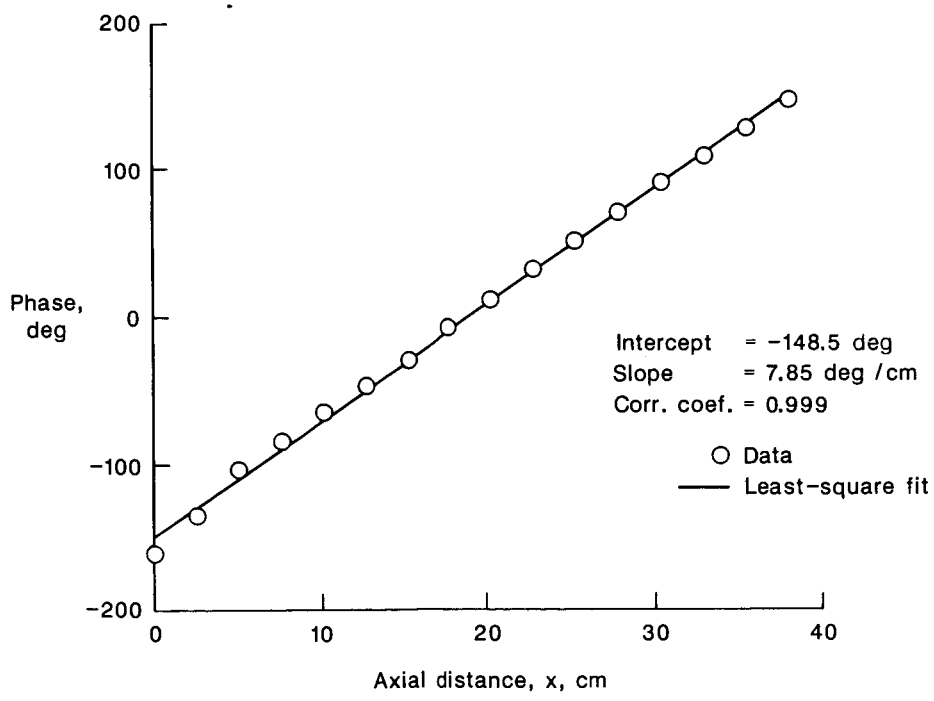

(b) Phase profile.

Figure 23. Measured axial acoustic pressure profile at Mach number of 0.3, frequency of 1.0 kHz, and upstream propagation.

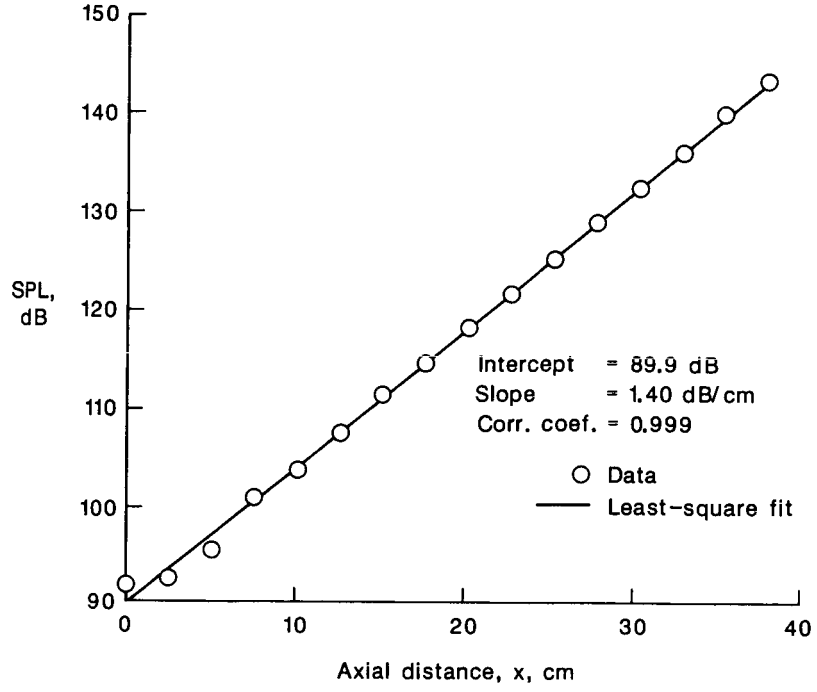

(a) Sound pressure level attenuation profile.

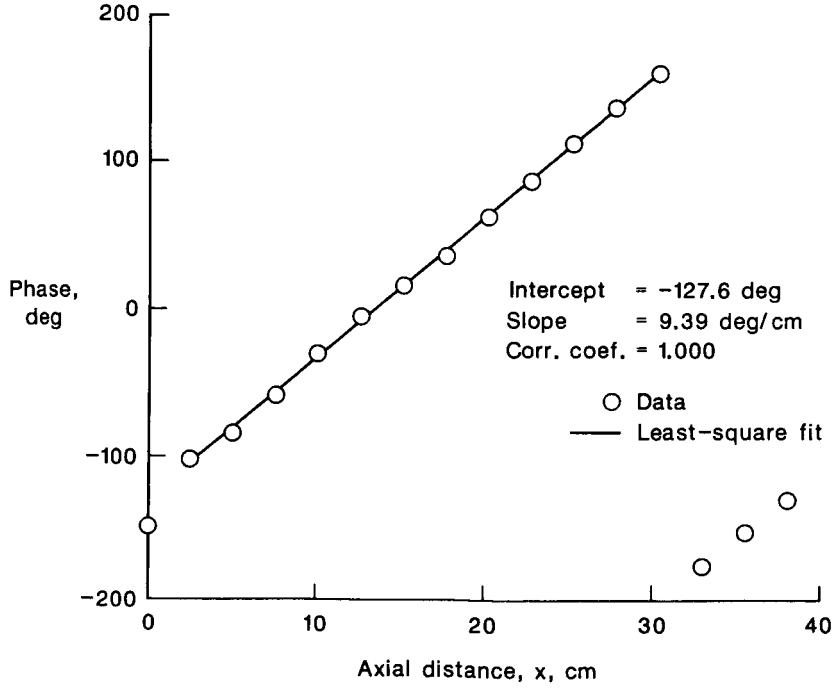

(b) Phase profile.

Figure 24. Measured axial acoustic pressure profile at Mach number of 0.5, frequency of 1.0 kHz, and upstream propagation.

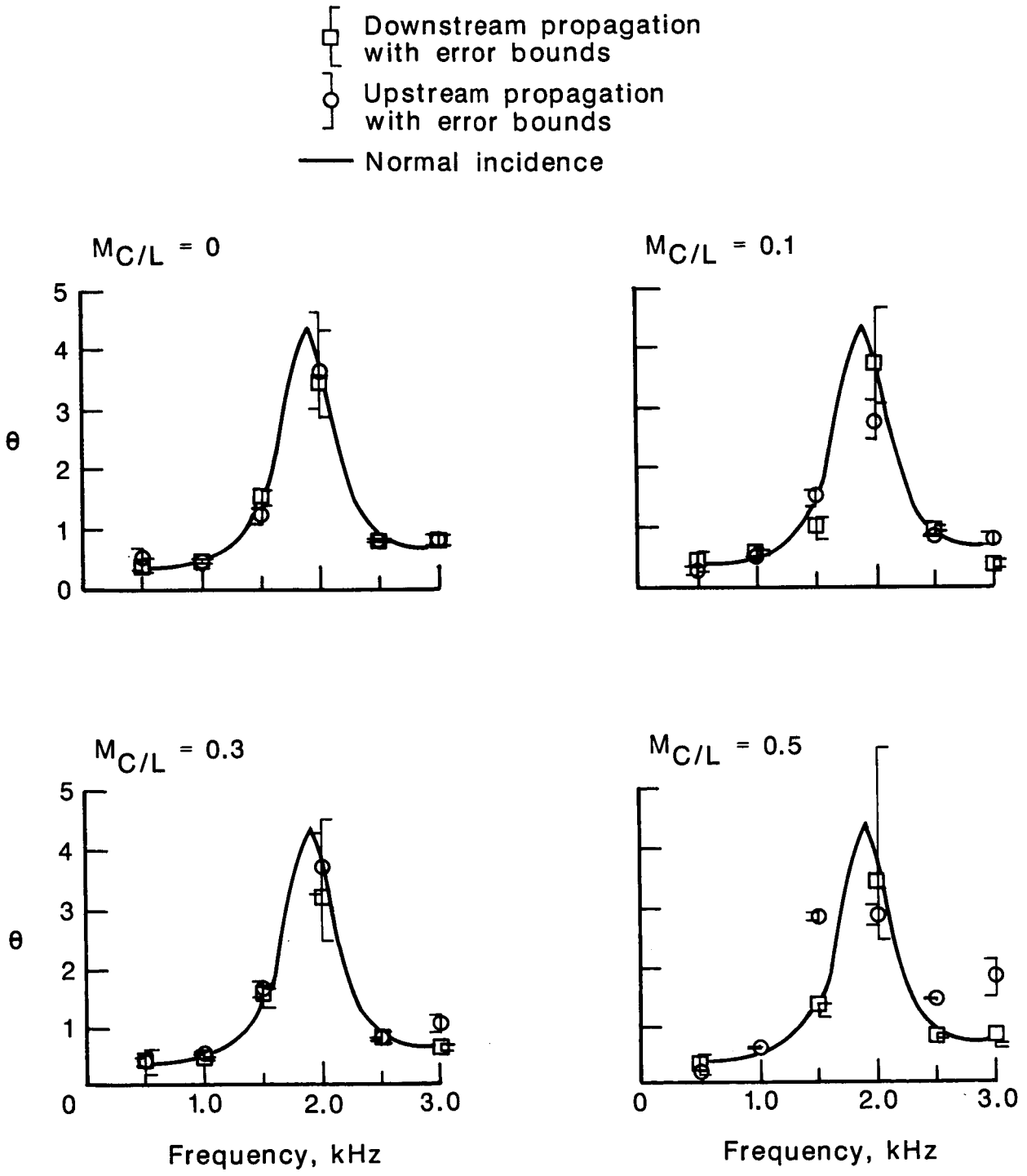

(a) Normalized acoustic resistance, θ.

Figure 25. Measured grazing-incidence impedance as inferred from uniform flow model.

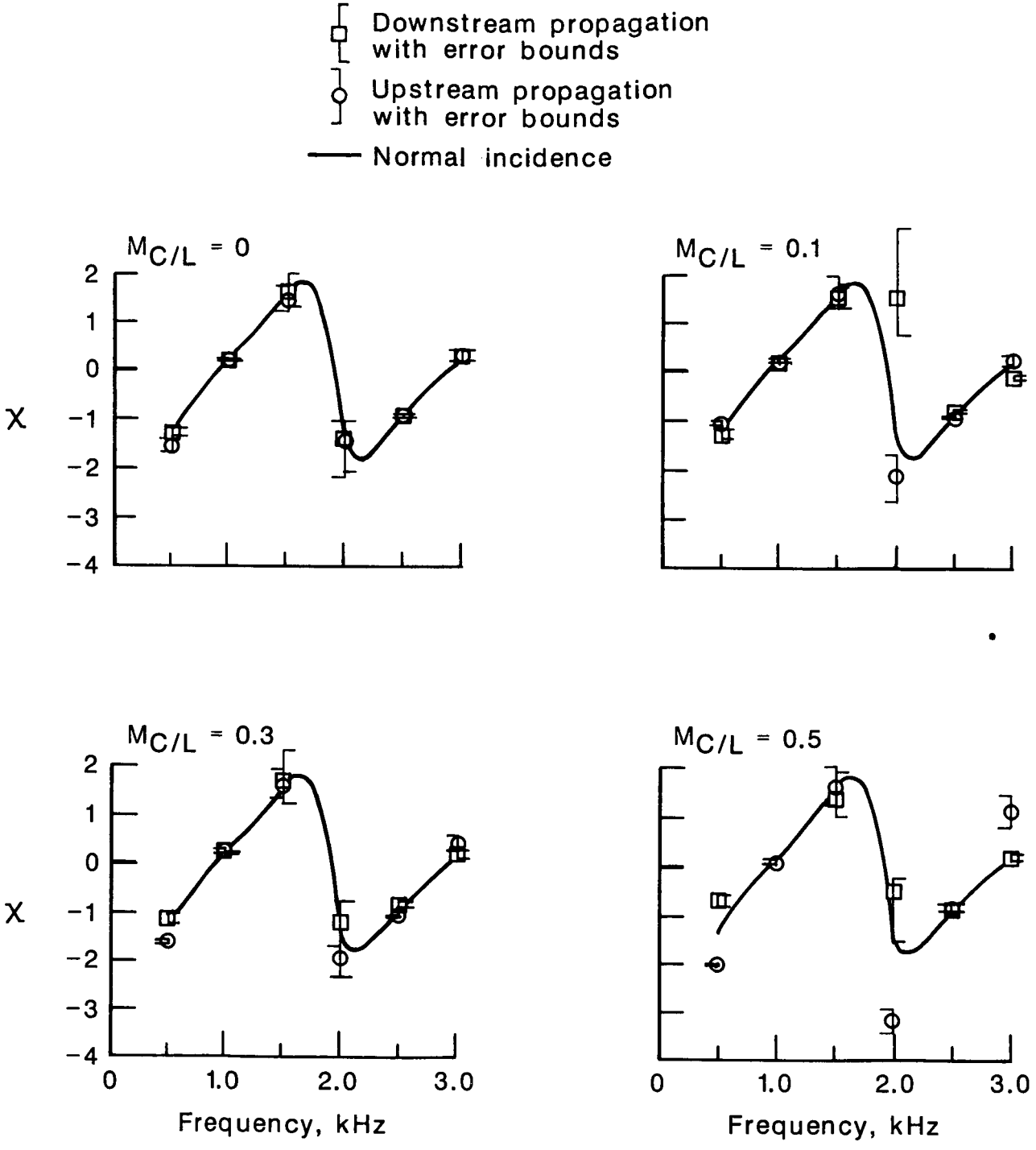

(b) Normalized acoustic reactance, χ.

Figure 25. Concluded.

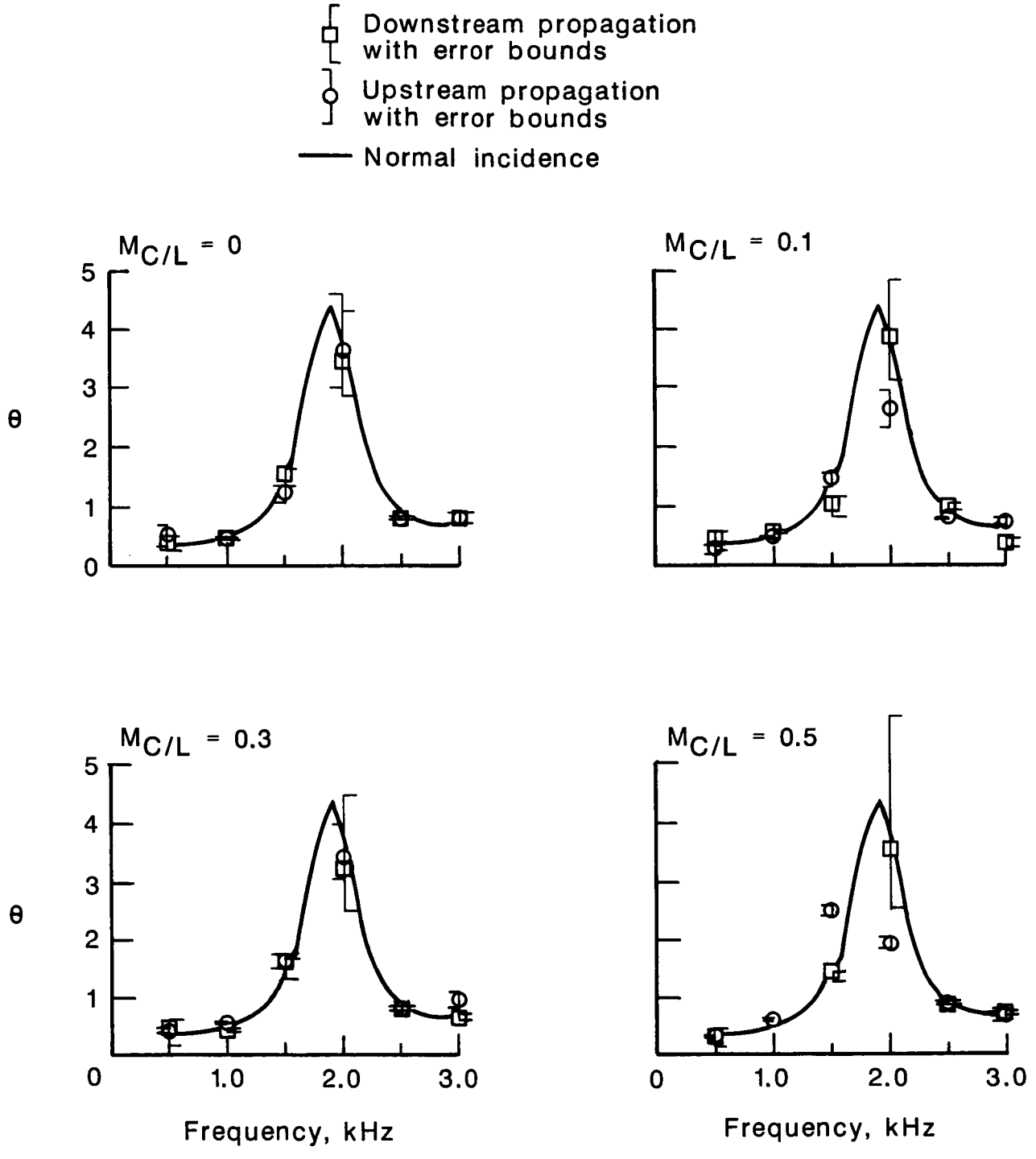

(a) Normalized acoustic resistance, θ.

Figure 26. Measured grazing-incidence impedance as inferred from one-dimensional shear-flow model.

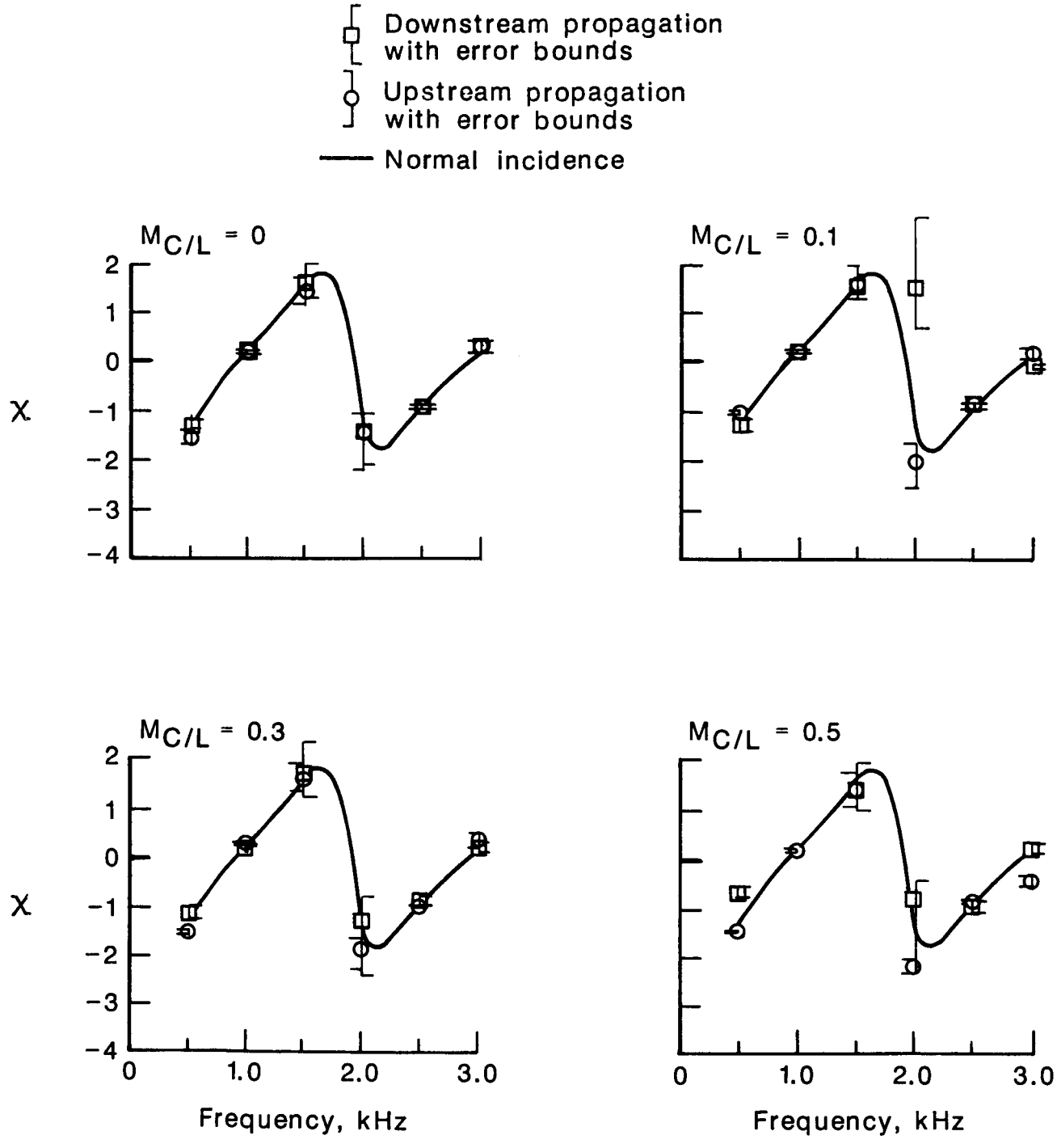

(b) Normalized acoustic reactance, χ.

Figure 26. Concluded.

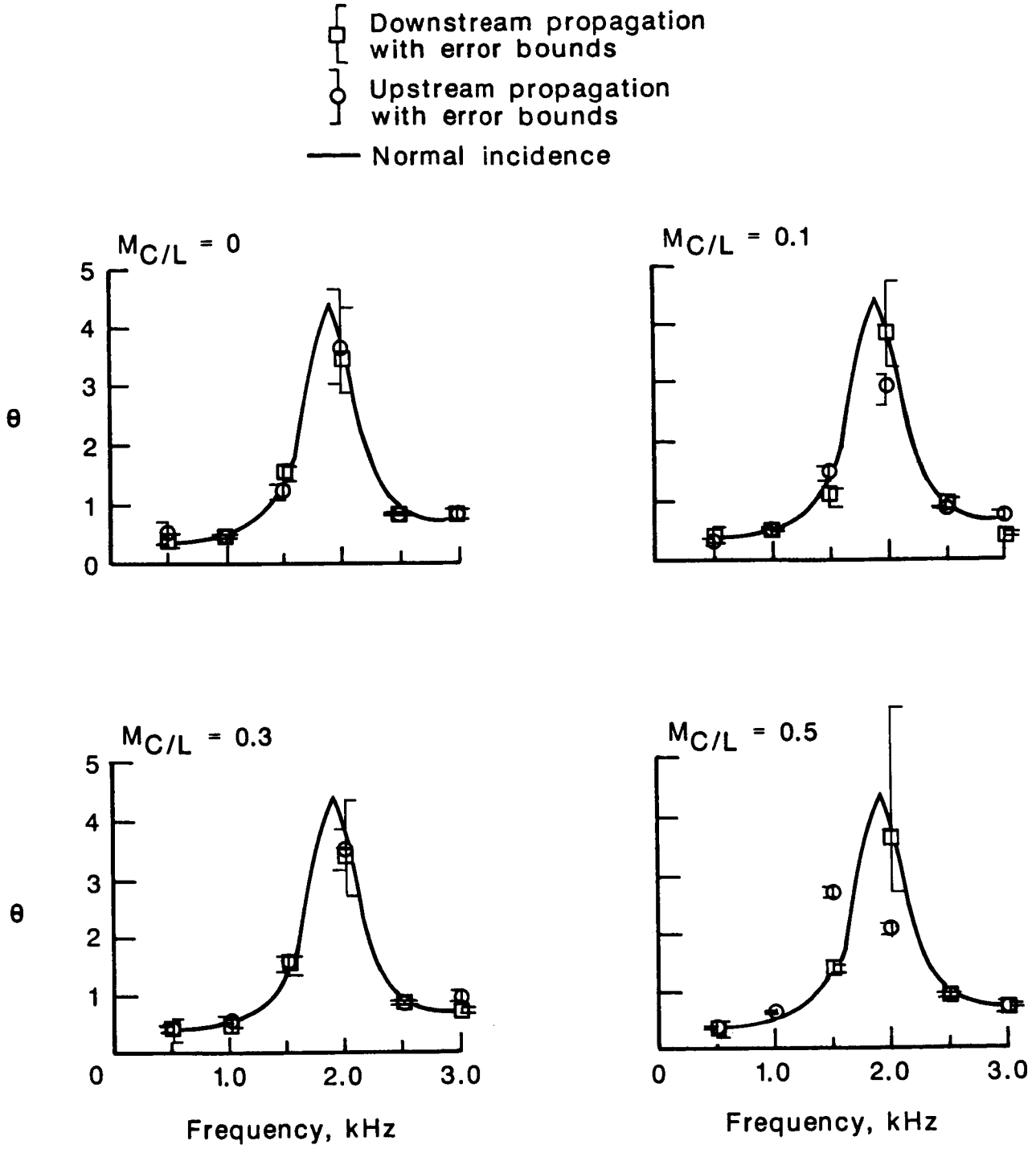

(a) Normalized acoustic resistance, θ.

Figure 27. Measured grazing-incidence impedance as inferred from two-dimensional shear-flow model.

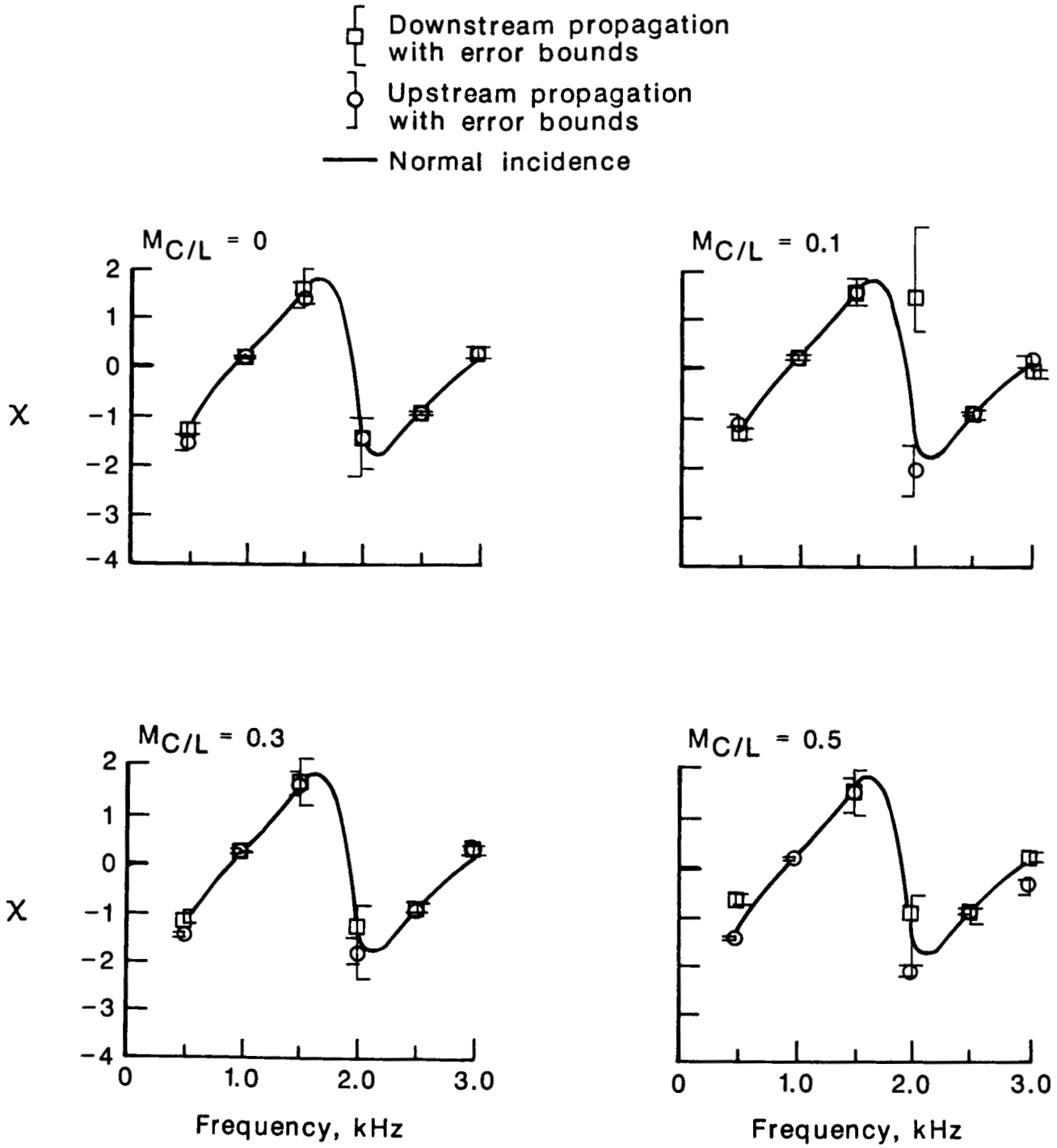

(b) Normalized acoustic reactance, χ.

Figure 27. Concluded.

NASA
National Aeronautics and Space Administration

Report Documentation Page

1. Report No.	2. Government Accession No.	3. Recipient's Catalog No.
NASA TP-2679		

4. Title and Subtitle	5. Report Date
Experimental Validation of a Two-Dimensional Shear-Flow Model for Determining Acoustic Impedance	May 1987
	6. Performing Organization Code
7. Author(s)	8. Performing Organization Report No.
Tony L. Parrott, Willie R. Watson, and Michael G. Jones	L-16203
9. Performing Organization Name and Address	10. Work Unit No.
NASA Langley Research Center Hampton, VA 23665-5225	505-61-11-02
	11. Contract or Grant No.
12. Sponsoring Agency Name and Address	13. Type of Report and Period Covered
National Aeronautics and Space Administration Washington, DC 20546-0001	Technical Paper
	14. Sponsoring Agency Code

15. Supplementary Notes

Tony L. Parrott and Willie R. Watson: Langley Research Center, Hampton, Virginia.
Michael G. Jones: PRC Kentron, Inc., Hampton, Virginia.

16. Abstract

Tests were conducted to validate a two-dimensional shear-flow analytical model for determining the acoustic impedance of a liner test specimen in a grazing-incidence, grazing-flow environment. The tests were limited to a test specimen chosen to exhibit minimal effects of grazing flow so that the results obtained by using the shear-flow analytical model would be expected to match those obtained from normal-incidence impedance measurements. Impedances for both downstream and upstream sound propagation were generally consistent with those from normal-incidence measurements. However, sensitivity of the grazing-incidence impedance to small measurement or systematic errors in propagation constant varied dramatically over the range of test frequencies.

17. Key Words (Suggested by Authors(s))	18. Distribution Statement
Acoustic impedance Admittance Shear flow Grazing incidence Grazing flow	Unclassified—Unlimited Subject Category 71

19. Security Classif.(of this report)	20. Security Classif.(of this page)	21. No. of Pages	22. Price
Unclassified	Unclassified	49	A03

NASA-Langley, 1987

For sale by the National Technical Information Service, Springfield, Virginia 22161-2171